Influence of extracellular polymeric substances (EPS) from Pseudomonas NCIMB 2021 on the corrosion behaviour of 70Cu–30Ni alloy in seawater

Blanca E. Torres Bautista, Agata J. Wikiel, Laryna Datsenko, Mario Vera, Wolfgang Sand, Antoine Seyeux, Sandrine Zanna, Isabelle Frateur, Philippe Marcus

Influence of extracellular polymeric substances (EPS) from *Pseudomonas* NCIMB 2021 on the corrosion behaviour of 70Cu-30Ni alloy in seawater

Blanca E. Torres Bautista[a], Agata J. Wikieł[b], Iaryna Datsenko[b], Mario Vera[b], Wolfgang Sand[b], Antoine Seyeux[a], Sandrine Zanna[a], Isabelle Frateur[a,c,d,*], Philippe Marcus[a]

[a]*PSL Research University, Chimie ParisTech, CNRS, Institut de Recherche de Chimie Paris, 75005, Paris, France*
[b]*Biofilm Centre, Aquatische Biotechnologie, Universität Duisburg-Essen, Universitätsstr. 5, 45141 Essen, Germany*
[c]*CNRS, UMR 8235, Laboratoire Interfaces et Systèmes Electrochimiques, F-75005, Paris, France*
[d]*Sorbonne Universités, UPMC Univ Paris 06, UMR 8235, LISE, F-75005, Paris, France*

**Corresponding author. e-mail: isabelle.frateur@upmc.fr*
Tel.: +33 1 44 27 72 15; fax: +33 1 44 27 40 74; postal address:
Laboratoire Interfaces et Systèmes Électrochimiques, UMR 8235 CNRS-UPMC, Université Pierre et Marie Curie, Case courrier 133, 4 place Jussieu, F-75252 Paris Cedex 05, France

Abstract

Copper alloys, often used in cooling circuits of industrial plants using seawater as coolant, can be affected by biocorrosion induced by biofilm formation. Extracellular polymeric substances (EPS) produced by bacteria play a fundamental role in the different stages of biofilm formation, maturation and maintenance. The influence of loosely bound (LB) and tightly bound (TB) EPS, extracted from marine *Pseudomonas* NCIMB 2021, on the electrochemical behaviour of 70Cu-30Ni (wt. %) alloy in static artificial seawater (ASW) and on the chemical composition of oxide layers was studied by combined electrochemical measurements (polarisation curves, EIS) and surface analysis (XPS, ToF-SIMS). Results were compared with those obtained in the presence of bovine serum albumin (BSA), a model protein. Compared to 70Cu-30Ni alloy in static ASW without biomolecules, for which a thick duplex oxide layer (outer redeposited Cu_2O layer and inner oxidized nickel layer) is shown, the presence of BSA, TB EPS and LB EPS leads to a mixed oxide layer (oxidized copper and nickel) with a lower thickness. In the biomolecules-containing solutions, this oxide layer is covered by an adsorbed organic layer, mainly composed of proteins. A model is proposed to analyse impedance data obtained at the corrosion potential. The fitting procedure of impedance diagrams allows extracting the anodic charge transfer resistance, from which the corrosion current density can be calculated. The results show a slow-down of the anodic reaction in the presence of biomolecules (BSA, TB EPS and LB EPS), and a corrosion inhibition effect by LB EPS and to a lesser extent by BSA. No detrimental effect is evidenced with TB EPS.

Keywords: copper alloy; seawater; biocorrosion; extracellular polymeric substances; EIS; surface analysis.

1 Introduction

Power plants require cooling circuits with seawater or fresh water as the cooling agent. Copper and copper alloys are commonly used in condensers and heat exchangers due to their high thermal and electrical conductivity, good mechanical workability and good resistance to corrosion. Those criteria have lead for a long time to the selection of copper alloys, such as aluminum brass, 70Cu-30Ni alloy and 90Cu-10Ni alloy, for their use in seawater [1-4]. Alloying nickel and small amounts of iron into copper improves the corrosion resistance; therefore, Cu-Ni alloys are preferred in marine environments due to the formation of a thin, adherent and protective surface film, which forms naturally and quickly upon exposure to clean seawater. That surface film is complex and predominantly made up of cuprous oxide, often containing nickel and iron oxides, cuprous hydroxychloride and cupric oxide; it becomes more complex when aggressive conditions from the water cause corrosion [2,5]. In cooling circuits, the water is usually circulating but, frequently, plant outages cause provisional stagnant condition that can persist for hours or, at worst, for days. Static conditions are of particular concern for corrosion risk, especially at the beginning of plant operation [5].

Cooling circuits of industrial plants are ideal incubators for microorganisms because they are aquatic environments, are maintained at temperatures between 30 and 60°C, at pH of 6 to 9, and provide a continuous source of nutrients, such as inorganic or organic compounds. The microorganisms present in cooling water circuits can be divided into planktonic or sessile cells. Sessile ones adhere to surfaces and form what is known as a biofilm. Biofilms are interface–associated colonies of microorganisms embedded in a self-produced organic polymeric matrix [6], containing molecules derived from the bulk aqueous phase and/or corrosion products of the metal substratum. Biofouling is hence a consequence of biofilm formation. The significant negative effects of biofouling are the blockage of water free flow in the cooling circuit and consequent mechanical damage to pumps, clogging of condenser tubes, reduction of the heat transfer efficiency and microbially induced corrosion (MIC) also called biocorrosion [7,8]. Additionally, Cu-Ni alloys are also chosen in seawater because of their resistance to biofouling; the reason for their antifouling behaviour is still not fully understood, but it may result from the action of a steady low level of cupric ions discharge [4]. Despite the copper toxicity, Cu alloys are vulnerable to MIC, especially when long periods of stagnation occur or when flow is intermittent. Differential aeration, selective leaching, under deposit corrosion, and cathodic depolarization have been reported as mechanisms for MIC of copper alloys [1,8,9].

Microorganisms are known to produce a great number of macromolecules (polysaccharides, proteins, lipids, DNA, humic substances and others), referred as extracellular polymeric substances (EPS), with various chemical and functional properties [10]. These exopolymeric components play a fundamental role in the different stages of biofilm formation, maturation and maintenance [11]. They are integral part of the biofilm matrix, mediating the cell adhesion to the surface, and promoting a strong binding of the microorganisms to each other. EPS, composed of macromolecules with varying hydrophilicity or having both hydrophilic and hydrophobic regions, can adhere to a wide range of surfaces [12]. In particular, the importance of extracellular proteins in the primary microbial attachment to the surface has been shown. The EPS matrix is also responsible for water retention. It maintains a highly hydrated microenvironment around biofilm microorganisms, enhancing their tolerance to desiccation in water-deficient environments. Exopolymers produced by the planktonic cells also should not be neglected, as they not only facilitate irreversible cell attachment but also

possess metal-binding capacity, which may lead to the formation of complexes with a range of redox potentials, probably participating in the electron-transfer processes that drive corrosion reactions [13,14].

EPS are organised around the cell in a particular way. Tightly bound (TB) EPS form capsules or sheaths associated closely with cell surfaces [15]; this is why they are also called capsular EPS [16,17]. Less compact, amorphous loosely bound (LB) EPS slime is dispersed to the more distant extracellular environment; some authors also use planktonic or free EPS to name such exopolymers [16,17].

The presence of EPS on the metallic surface can modify the morphology and chemistry of corrosion products, often giving these products more aggressive properties. Beech *et al.* characterised surface layers formed on AISI 316 stainless steel exposed to different types of EPS produced by *Pseudomonas* NCIMB 2021 (planktonic or free EPS, capsular EPS, and biofilm EPS); they observed differences in surface chemical composition, depending on the type of EPS [17]. Exopolymers secreted by adherent bacteria can enhance corrosion [18]. The capacity of EPS to bind metal ions and to form complexes is important to MIC [19], and depends both on the bacterial species and on the type of metal ion. Some data supporting the idea of a corrosion promoting effect of EPS have been published [20,21]. Some proposed MIC models also describe the potential involvement of sulphate reducing prokaryotes (SRP) exopolymers in metal deterioration [14]. Subsequently, the importance of reactions mediated by EPS proteins (enzymes) has started to be also considered as relevant to biocorrosion [22].

From the other side, a low number of publications concerning microbially influenced corrosion inhibition (MICI) can be found. A protective role of EPS due to hindering of the corrosion products diffusion from the metal surface has been reported [23]. A first evaluation of the suitability of EPS produced by several bacterial strains, including sulphate-reducing bacteria (SRB) and *Pseudomonas*, for corrosion protection of metallic substrates (pure iron, carbon steel and 304 stainless steel) confirmed that some of them might possess candidate compounds to be potentially used for a further development of green corrosion mitigation strategies [24]. Recently, the role of *Desulfovibrio alaskensis* EPS in the biocorrosion initiation or inhibition of carbon steel in marine environment was studied [25,26].

The contents of macromolecules (proteins, sugars, DNA, uronic acids) for a given EPS vary with the bacterial species, the type of EPS (planktonic or free EPS, capsular EPS, biofilm EPS), and the growth conditions [16,17,27]. In addition, it is important to mention that a universal procedure for EPS extraction does not exist as the properties of exopolymers and, especially the susceptibility of different bacterial cells to extraction reagents, can differ; the EPS isolation efficiency might differ, resulting in a variable EPS composition [28-30]. Therefore, the quality of each investigation concerning EPS depends greatly on the development and use of a proper extraction procedure.

Further investigations must be performed to bring new insights on the role of EPS in corrosion processes and to provide comprehensive characterization of its compounds. These data will be useful for understanding the mechanisms of metal-microorganism interactions mediated by these EPS. In the future, they may likewise provide a necessary background for developing new strategies for biocorrosion prevention.

In this context, the objective of this work was to study the effect of LB EPS and TB EPS extracted from a marine aerobic strain of *Pseudomonas*, *Pseudomonas* NCIMB 2021, on the

electrochemical behaviour of 70Cu-30Ni (wt. %) alloy and the chemical composition of oxide layers in artificial seawater (ASW), in static conditions. *Pseudomonas* NCIMB 2021 was originally isolated by Fletcher and Floodgate [31] and has been employed in several cell attachment and exopolymer-production studies [32-36]. Results were compared with those obtained in ASW added with bovine serum albumin (BSA), a model protein often used to study the protein-surface interactions due to its low cost and to a good knowledge of its properties [37-39]. The effect of BSA adsorption on the corrosion behaviour of 70Cu-30Ni alloy in static ASW was the subject of a previous paper [40]. For that purpose, electrochemical measurements (corrosion potential E_{corr} *vs* time, polarization curves and electrochemical impedance spectroscopy (EIS)) performed during the very first steps of oxide layers formation (1 h immersion time) were combined to surface analysis by X-ray photoelectron spectroscopy (XPS) and time-of-flight secondary ions mass spectrometry (ToF-SIMS). Although 1 h immersion time is a short time for the formation of oxides, it is not a short time for the adsorption of proteins, such as BSA, since an adsorption plateau (steady-state) is reached within 10-20 min [39,41,42].

2 Experimental

2.1 Metallic material, electrolyte

The material under study was 70Cu-30Ni alloy (Cu 68.5, Ni 30, Mn 0.8, Fe 0.7 wt. %). The samples provided by RSE S.p.A. were disks cut from real new condenser tubes, and then flattened at Chimie ParisTech. The geometrical surface area exposed to the solution was 0.45 cm^2, and the tightness between the disk and the sample holder was ensured by a Viton® O-ring. Before electrochemical measurements, samples were mechanically polished with SiC papers down to grade 1200, then degreased in an ultrasonic bath three times in acetone for 10 min, once in ethanol for 10 min, and once in ultra-pure water for 10 min, dried under an argon flow, and finally exposed to UV for 20 min. Before surface analysis, samples were mechanically polished first with SiC papers down to grade 1200, then with 6 µm, 3 µm, and 1 µm diamond pastes; their subsequent treatment was the same as before electrochemical measurements.

The used solution was aerated artificial seawater (ASW; composition (g/L): NaCl (24.615), KCl (0.783), Na_2SO_4 (4.105), $MgCl_2$ $(H_2O)_6$ (11.060), $CaCl_2$ (1.160), $NaHCO_3$ (0.201); pH = 8.0), without and with biomolecules.

2.2 Biomolecules

In a first step, the effect of bovine serum albumin (BSA) on the corrosion behaviour of 70Cu-30Ni alloy in seawater was evaluated. BSA is a model protein, with a molecular weight of ~ 66 kDa *(i.e.* 66 $kg.mol^{-1}$), which is often used to study protein-surface interactions. The concentration of BSA (~99% purity (Fraction V); Sigma Aldrich) in solution was 20 $mg.L^{-1}$.

In a second step, the effect of tightly bound (TB) and loosely bound (LB) extracellular polymeric substances (EPS) secreted by *Pseudomonas* NCIMB 2021 marine strain was studied. The EPS extraction procedure, which was developed at the Biofilm Centre, University of Duisburg-Essen, Germany, is illustrated in Figure 1 [26]. *Pseudomonas* NCIMB 2021 was grown in 5 L fresh Marine Broth 2216 growth medium (37.4 $g.L^{-1}$) for 3 days under constant aeration. Medium sterilisation was achieved by autoclaving at 121°C for 30 min. The medium was inoculated with 5% (v/v) *Pseudomonas* NCIMB 2021 suspension in exponential growth phase (initial cell number: 10^7 $cells.mL^{-1}$), and incubated for 3 days at 30°C, with

gentle agitation. Once the bacteria reached the exponential growth phase, EPS extraction was performed. The batch culture was centrifuged at 4°C, 6500 × g for 12 min, to isolate LB EPS. After centrifugation, the supernatant was separated from the pellet and twice sterile filtered through 0.22 µm pore size Whatman® GD/X syringe filters. In order to remove metabolites and salts of low molecular weight, filtered supernatant was dialysed overnight at 4°C using Spectra/Por 3.5 kDa dialysis tubing. This purification was performed either in deionised water for colorimetric assays (EPS composition analyses) or in ASW for electrochemical measurements and surface analysis. The dialysis was continued for additional 48h at 4°C, under stirring at 100 rpm. Water was changed 3 times a day. Harvested cell pellet was washed with ASW in order to remove residues from the growth medium. For the tightly bound EPS extraction, the Dowex Marathon™C cation exchange resin, Na^+ form, 20–50 mesh size, was used [43].
In order to determine the bulk composition of EPS secreted by *Pseudomonas* NCIMB 2021, colorimetric analyses were carried out, at least in triplicates for each determined parameter, using chemicals of analytical grade. For the determination of absorbance, Varian Cary 50 Bio UV/Visible spectrophotometer was used. Absorbance was measured against deionised water, and converted to concentration by use of calibration standards for each method. Phenol–sulphuric acid method was used for the determination of polysaccharide content [44], with glucose as a standard. Uronic acids levels were determined as described by Filisetti-Cozzi and Carpita [45], with glucuronic acid as a standard. Extracellular DNA was determined as described by Burton [46], with DNA from salmon sperm as a standard. Protein concentration was estimated as described by Bradford [47], with BSA as a standard. In order to determine the cell lysis level in extracted EPS, the 2-keto-3-deoxyoctanate (KDO) concentration was determined as described elsewhere [48,26], with KDO as a standard. Cell damage was performed according to Aljanabi and Martinez [49] with heating at 60°C for 1 h.

For electrochemical measurements and surface analysis, ASW solutions were prepared with the secreted TB and LB EPS, keeping the same protein concentration as for the BSA-containing solution (20 $mg.L^{-1}$), in order to compare the results with those obtained in the presence of the model protein. Thus, LB EPS aliquots were used as isolated *i.e.* were not diluted (protein concentration after isolation: 20.6 $mg.L^{-1}$), whereas TB EPS aliquots were diluted about 200 times in ASW (protein concentration after extraction: ~ 4190 $mg.L^{-1}$).

2.3 Electrochemical measurements

The electrochemical measurements were performed with a three-electrode cell, designed and manufactured at Chimie ParisTech, with a solution volume of about 0.1 L. The working electrode was the 70Cu-30Ni alloy (disk samples), the counter-electrode was a platinum wire, and the reference electrode was a saturated calomel electrode (SCE; 0.245 V *vs* SHE). Experiments were carried out at room temperature and in stagnant conditions (static working electrode and solution).

The corrosion potential (E_{corr}) was measured during the first hour of immersion, then cathodic or anodic polarization curve was plotted separately starting from +20 or -20 mV *vs* E_{corr}, respectively, using a scan rate of 0.5 $mV.s^{-1}$. Electrochemical impedance diagrams were plotted at E_{corr} after 1 h of immersion, with a frequency domain ranging from 10^5 Hz to 10^{-3} Hz, 7 points per decade, and an amplitude of 10 mV peak-to-peak. Electrochemical measurements were performed with an EC-Lab SP-200 system from Bio-Logic.

2.4 Surface analysis

Four 70Cu-30Ni samples were analyzed by XPS and ToF-SIMS after 1 h of immersion at E_{corr} in static ASW 1) without biomolecules, 2) with 20 mg.L^{-1} of BSA, 3) with TB EPS (protein concentration: 20 mg.L^{-1}), and 4) with LB EPS (protein concentration: 20 mg.L^{-1}).In the following, these samples will be named ASW, ASW + BSA, ASW + TB EPS, and ASW + LB EPS, respectively. After the electrochemical measurements, the samples were gently dipped in ultra-pure water three times to remove the biomolecules weakly bound to the alloy surface, then dried with argon before introduction in the fast-entry lock chamber of the XPS spectrometer.

XPS analyses were performed with a Thermo Electron Escalab 250 spectrometer, using a monochromatised Al Kα X-ray source (1486.6 eV). The analyser pass energy was 100 eV for survey spectra and 20 eV for high resolution spectra. The spectrometer was calibrated using Au $4f_{7/2}$ at 84.1 eV. The following core levels were recorded: Cu 2p (and Auger lines), Ni 2p, O 1s, C 1s, and N 1s. All spectra were referred to the C 1s peak for the carbon involved in C-C and C-H bonds, located at 285 eV. Curve fitting of the spectra was performed with the Thermo Electron software "Avantage".

ToF-SIMS analyses were done using a ToF-SIMS V spectrometer (ION-TOF GmbH). The analysis chamber was maintained at less than 10^{-9} Pa in operation conditions. The depth profiles were performed using the instrument in dual beam mode. A pulsed 25 keV Bi^+ primary ion source (LMIG) at a current of 1.2 pA (high mass resolution mode), rastered over a scan area of 100×100 µm², was used as the analysis beam. The sputtering was performed using a 1 keV Cs^+ ion beam at a current of 50 nA, and rastered over an area of 300×300 µm² (for ASW, ASW + BSA and ASW + TB EPS) or 700×700 µm² (for ASW + LB EPS). The depth profiles were obtained in negative polarity meaning only negative ions were analysed. The distribution of the ionized fragments, all measured quasi-simultaneously, were plotted versus Cs^+ ion sputtering time. The intensity was reported using a logarithmic scale, which gave equal emphasis to signals of all intensities. The variation of the ion intensity with sputtering time reflects the variation of the in-depth concentration but is also dependent on the matrix from which the ions are emitted. For the estimation of the oxide layer thickness, two cases were considered: (1) for a layer composed of one single metallic oxide, the thickness was assessed from the theoretical sputtering rate of the corresponding pure metal (given in tables) in the same sputtering conditions, and (2) for a mixed oxide layer, the thickness was estimated from an average sputtering rate calculated from the sputtering rates of pure metals multiplied by the fraction of each element in the oxide. Data acquisition and processing were performed using the IonSpec software.

3 Results

3.1 Bulk composition of EPS

The bulk composition of EPS from *Pseudomonas* NCIMB 2021, deduced from colorimetric analyses, is shown in Table 1. The KDO concentration indicates that cell lysis level in extracted EPS is less than 1%. The composition of the negative control (sterile growth medium) is also given for comparison. In this table, proteins appear to be the main components of TB EPS, whereas sugars seem to be dominant in LB EPS and in the negative control. Sugars content was ten times higher than proteins content in the negative control while this ratio was about 2.5 in LB EPS. Our results are in agreement with those found by Beech *et al.* who characterised planktonic, capsular and biofilm EPS of *Pseudomonas*

NCIMB 2021 [17]. They showed that the content and the ratio of macromolecules (proteins, sugars and uronic acids) in the bulk phase differed depending on the type of EPS. In particular, they concluded to a significantly higher amount of proteins contained in capsular EPS compared to planktonic EPS.

SDS-PAGE profiles of extracellular proteins present in exopolymers produced by *Pseudomonas* NCIMB 2021 were previously studied [16]. In the loosely bound EPS fraction, four bands of 100, 60, 50 and 34 kDa were found, while in the tightly bound fraction, around 12 bands between 25 and 100 kDa could be observed. Thus, the molecular weights of proteins present in TB and LB EPS (25 – 100 kDa) are comparable to that of BSA (66 kDa).

3.2 Electrochemical measurements

During the first hour of immersion in ASW, the corrosion potential of 70Cu-30Ni alloy decreases till reaching a plateau. The different E_{corr} steady-state values after 1 h of immersion without and with biomolecules are shown in Table 2. The corrosion potential is similar for the three biomolecules and is more cathodic in the absence of biomolecules (difference of ~30 mV).

The cathodic polarisation curves of 70Cu-30Ni alloy recorded in the different solutions are presented in Figure 2(a). In all cases, except with LB EPS, two plateaus can be observed: a short plateau close to E_{corr} that illustrates the first step of dissolved oxygen reduction (transfer of 2 electrons), and a wide plateau for potentials ranging from -0.40 to -1.00 V *vs* SCE corresponding to the second step of O_2 reduction (transfer of 4 electrons). It is well-known that this reaction is limited by mass transport. Only the second plateau is clearly visible in the presence of LB EPS.
The presence of biomolecules induces lower current densities in the second plateau potential domain. Compared with ASW ($|j| \sim 40$ µA.cm^{-2}), the plateau current density is divided by 2 in the presence of BSA ($|j| \sim 20$ µA.cm^{-2}), by 1.5 in the presence of TB EPS ($|j| \sim 27$ µA.cm^{-2}) and by 3.3 with LB EPS ($|j| \sim 12$ µA.cm^{-2}). Therefore, there is an effect of biomolecules on the cathodic behaviour of 70Cu-30Ni alloy.

The anodic polarisation curves of 70Cu-30Ni alloy in the same solutions are presented in Figure 2(b). The presence of biomolecules induces lower current densities for potentials lower than 0.05 V *vs* SCE. Above 0.05 V *vs* SCE, all the curves exhibit the same shape and current densities except that with LB EPS, for which the current densities are lower up to 0.25 V *vs* SCE and the curve reveals some peaks between 0.25 and 0.5 V *vs* SCE.
An effect of the rotation speed on the anodic polarisation curves plotted with a rotating ring electrode was evidenced below 0.3 V *vs* SCE (results not shown here). However, the curves exhibit no anodic plateau unlike pure copper in acidic and neutral chloride solution for which a limiting-current region can be observed around 0 V *vs* SCE [50,51]. These results show partial mass transport limitation *i.e.* mixed kinetics for the anodic partial reaction(s) at not too high anodic potential.

The impedance diagrams plotted after 1 h of immersion at E_{corr} in static ASW without and with biomolecules are shown in Figure 3. The shape is the same in all cases and two loops can be observed: one depressed high frequency (HF) loop and one not well defined low frequency (LF) loop. The size of the HF loop in the presence of TB EPS is the same as that without biomolecules. However, it is slightly higher in the presence of BSA, and much higher in the presence of LB EPS. The impedance diagrams were plotted at E_{corr}, which is not the same in

the different solutions. Therefore, the analysis of data must take into account the effect of potential (see § 4.1).

3.3 Surface analysis

A characteristic ToF-SIMS depth profile (negative ions) obtained on 70Cu-30Ni alloy immersed during 1 h at E_{corr} in ASW without biomolecules is presented in Figure 4(a). The $^{18}O^-$ isotopic signal, characteristic of the oxide layer, is used since the extremely intense $^{16}O^-$ (main isotope) signal saturates the detector. This profile evidences a stratification of the oxide film covering the metallic surface. Three regions can be observed. The first one extends from 0 s to 200 s of sputtering, characterized by an intense $95^{63}CuO_2^-$ signal. As one probes deeper into this first region, a progressive increase of the $90^{58}NiO_2^-$ signal is observed, indicating that the outer oxide layer is mainly composed of copper oxide, with the presence of some Ni oxide and/or hydroxide (denoted I in Figure 4(a)). In the second region (II in Figure 4(a)) that extends from 200 s to 290 s, a sharp decrease of the $95^{63}CuO_2^-$ signal is observed, whereas $90^{58}NiO_2^-$ signal reaches its maximum intensity. This second region is assigned to a nickel oxide and/or hydroxide inner layer in which the presence of oxidized copper cannot be excluded. Finally, after 290 s of sputtering, one enters the third region (III in Figure 4(a)) characterized by a sharp decrease of all oxidized signals ($18^{18}O^-$, $95^{63}CuO_2^-$ and $90^{58}NiO_2^-$) and a constant and intense plateau for the $116^{58}Ni_2^-$ signal, which is characteristic of the metallic substrate. It is noticeable that Cl species (represented by the $35Cl^-$ signal on the profile) are present essentially in the outer part of the oxide layer (copper oxide). Thus, the oxide film formed on 70Cu-30Ni alloy in ASW without biomolecules exhibits a duplex structure with (i) a 20 nm-thick outer layer mainly composed of copper oxide and (ii) a 10 nm-thick inner layer mainly composed of oxidized nickel.

Figure 4(b) shows the ToF-SIMS negative depth profile obtained with 70Cu-30Ni after 1 h of immersion in ASW with 20 $mg.L^{-1}$ of BSA. In this figure, it is possible to distinguish mainly four regions. The first region, that goes from 0 to 10 s, shows an increase of all the signals, and it is characterised by a maximum intensity of the $35Cl^-$ and $26CN^-$ (characteristic signal of proteins -peptidic link-) signals. From 10 s up to 25 s of sputtering, the second region is observed, where the $95^{63}CuO_2^-$, $18^{18}O^-$ and $90^{58}NiO_2^-$ signals reach their maximum intensity, and the $35Cl^-$ and $26CN^-$ signals sharply decrease. This second region corresponds to the oxide layer not covered by the BSA. In the third region, from 25 s up to 64 s of sputtering, the $95^{63}CuO_2^-$, $18^{18}O^-$, $35Cl^-$ and the $90^{58}NiO_2^-$ signals form a shoulder, whereas the $26CN^-$ signal keeps sharply decreasing and the $116^{58}Ni_2^-$ signal gradually increases. This third region evidences the oxide layer beneath the BSA layer. Finally after ~ 64 s of sputtering, the oxide signals exhibit a sharp decrease, and the $116^{58}Ni_2^-$ signal forms a plateau indicating that the alloy/oxide interface is reached. By ToF-SIMS, it is not possible to identify a stratification of the different compounds on the alloy surface in the presence of the protein. The depth profile shows one mixed oxide layer (oxidized copper and nickel) with a thickness of ~ 10 nm, being three times lower than that in the absence of the protein, and partly covered by the BSA layer.

ToF-SIMS depth profiles (negative ions) were also performed on 70Cu-30Ni after 1 h of immersion in ASW in the presence of TB (Figure 4(c)) and LB (Figure 4(d)) EPS. The oxide layer formed on the alloy exposed to LB EPS is very thin, and the profile was performed using a higher sputtering area (700 x 700 μm^2) (other conditions remaining unchanged) in order to have a better in-depth resolution (Figure 4(d)). Similarly to the ToF-SIMS profiles described previously, the position of the metal/oxide interface is located from the decrease of the oxidized signals intensity ($95^{63}CuO_2^-$, $18^{18}O^-$ and $90^{58}NiO_2^-$) and the increase of the metallic signal ($116^{58}Ni_2^-$). It can be observed that whatever the kind of EPS (TB or LB), a mixed Cu and Ni oxide layer (II in Figures 4(c) and (d); no oxide stratification) covers the

metallic substrate (III in Figures 4(c) and (d)), with a much thinner oxide film on the surface exposed to LB EPS compared to the one exposed to TB EPS. In both profiles, the oxide film is covered by an organic layer, assigned to the presence of TB or LB EPS (I in Figures 4(c) and (d)), as indicated by the intense $26CN^-$ and $63PO_2^-$ signals that reach a maximum intensity before the signals assigned to oxide species ($95^{63}CuO_2^-$, $18^{18}O^-$ and $90^{58}NiO_2^-$). Moreover, sulphur is present throughout the entire oxide layer, as indicated by the $32S^-$ signal that decreases around the alloy/oxide interface. The link between the TB or LB EPS and the oxide is likely made by the sulphur and the phosphorus present in the biomolecules, as indicated by the maximum intensity of the $32S^-$ and $63PO_2^-$ signals that is located in between the maximum intensity of the biomolecules signal ($26CN^-$) and that of the oxide signals ($95^{63}CuO_2^-$, $18^{18}O^-$ and $90^{58}NiO_2^-$).
From the recorded ToF-SIMS profiles, it can be observed that biomolecules (BSA, TB or LB EPS) are adsorbed on the surface. They do not prevent the formation of an oxide film underneath, covering the 70Cu-30Ni alloy. The presence of biomolecules drastically modifies (i) the thickness of the oxide film, according to the following sequence of thickness: ASW > ASW + BSA > ASW + TB EPS > ASW + LB EPS, and (ii) the structure and composition of the oxides since a mixed Cu and Ni oxide layer is observed in the presence of biomolecules, whereas a duplex structure with an outer Cu oxide layer covering an inner Ni oxide layer is evidenced in the absence of biomolecules. At last, the ToF-SIMS data show that the amount of Cl^--containing species in the adsorbed layer is lower in the presence of TB EPS or LB EPS compared to that with BSA.

The chemical composition of surface layers formed on the 70Cu-30Ni alloy was investigated by XPS after 1 h of immersion in static ASW without biomolecules (ASW) and with BSA (ASW + BSA), TB EPS (ASW + TB EPS) and LB EPS (ASW + LB EPS). The corresponding XPS spectra of Cu $2p_{3/2}$, Cu Auger, Ni $2p_{3/2}$, N 1s, C 1s and Cl 2p are shown in Figure 5.
The decomposition of the Cu $2p_{3/2}$ XPS region into different chemical states is difficult because the Cu^0 and Cu^+ signals are located at the same binding energy (932.3 eV). This difficulty is overcome by making use of the Cu Auger line ($L_3M_{45}M_{45}$), helpful for distinguishing these two species [52-58]. After immersion in ASW, the XPS Cu $2p_{3/2}$ core level peak with a binding energy located at 932.3 eV (Figure 5(a)) and the Cu Auger line ($L_3M_{45}M_{45}$) at a kinetic energy of 916.4 eV (Figure 5(b)) demonstrate the presence of Cu^+ as shown previously [40]. After immersion in ASW with biomolecules, the first peak at 932.2 eV corresponds to Cu^+ and/or Cu^0, and the second peak at higher binding energy, 934.0 eV, with a satellite at 944.0 eV, corresponds to Cu^{2+}. The position of the Auger line ($L_3M_{45}M_{45}$) (Figure 5(b)), at a kinetic energy of 917.4 eV for ASW + BSA and ASW + TB EPS, is probably due to a major contribution of Cu^{2+}. In contrast, for ASW + LB EPS, the Auger line at 919.2 eV indicates a major contribution of Cu^0.
The XPS Ni $2p_{3/2}$ core level spectra recorded in the presence of biomolecules exhibit a peak at a binding energy of 856.0 eV and the corresponding satellite at 861.7 eV, showing the presence of $Ni(OH)_2$ in the surface layer (Figure 5(c)). For LB EPS, significant difference is observed: there is a peak at a binding energy of 852.2 eV characteristic of Ni^0. The presence of metallic components of Cu and Ni for the sample after immersion in ASW + LB EPS indicates that the oxide layer is much thinner than the ones formed in static ASW, ASW + BSA, and ASW + TB EPS (for which the metallic components are not present). The XPS Cl 2p core level spectra are shown in Figure 5(d). A peak centred at 198.6 eV is observed on the alloy exposed to ASW and ASW + BSA. Using the intensity of the Cl 2p signal for the sample immersed in ASW, the amount of Cl^- can be calculated; a value of ~ 0.2 % is found. The Cl 2p signal intensity is similar after immersion in ASW + BSA, whereas there is nearly no Cl detected by XPS on the sample exposed to ASW + TB EPS or ASW + LB EPS.

The N 1s spectra recorded after immersion in ASW with biomolecules (Figure 5(e)) exhibit a major symmetrical peak, centred at 400.2 eV, as expected for the amine or amide groups of proteins [59,39,41]. The C 1s signals obtained in the same conditions are shown in Figure 5(f). The signal at low binding energy observed after immersion in ASW without biomolecules is assigned to surface contamination. C 1s peak can be fitted with three contributions corresponding to well identified carbon bonds: C_1, at a binding energy of 285.0 eV, assigned to **C**-C and **C**-H; C_2, at a binding energy of 286.4 eV, attributed to **C**-N and **C**-O single bonds; and C_3, at a binding energy of 288.3 eV, assigned to O=**C**-O and O=**C**-N (peptide bonds) bonds [59,60,39].

The "nitrogen/carbon" and "carbon/carbon" atomic ratios were calculated from the N 1s and C 1s signals. The atomic ratio X/Y is given by: $X/Y = I_X\sigma_Y\lambda_Y T_Y / I_Y\sigma_X\lambda_X T_X$, where $I_{X,Y}$ is the intensity of the peak (peak surface area) associated to element X or Y (X and Y being N or C), $\lambda_{X,Y}$ the attenuation length in the biomolecule layer of photoelectrons emitted by the X or Y 1s core level, $\sigma_{X,Y}$ the photoionization cross-section of X 1s or Y 1s, and $T_{X,Y}$ the transmission function of X 1s or Y 1s. The values of these ratios obtained for the 70Cu-30Ni alloy immersed in static ASW without and with biomolecules, as well as those estimated in previous studies for the BSA powder [41,61] are presented in Table 3. The good agreement between the values for the sample exposed to BSA and the BSA powder provides a fingerprint for the protein, and allows us to conclude that the protein is adsorbed on the surface. The relatively good agreement between the values obtained for the two EPS solutions and the BSA powder shows that adsorbed proteins are the main biomolecules present on the alloy surface. However, with TB EPS, some deviations are observed due to the presence of other biomolecules on the surface.

In the case of ASW + BSA, the thickness of the adsorbed BSA layer d_{BSA} can be calculated from the $I_N^{BSA} / I_{Cu}^{Oxide}$ ratio. The nitrogen signal comes only from the protein and is therefore a fingerprint of the adsorbed protein. The N 1s intensity emitted by the adsorbed BSA is given by:

$$I_N^{BSA} = k\sigma_N\lambda_N^{BSA}D_N^{BSA}T_N\left[1-\exp\left(-\frac{d_{BSA}}{\lambda_N^{BSA}}\right)\right] \quad (1)$$

where k is the spectrometer specific constant, and D_N^{BSA} the nitrogen density in the BSA layer. The Cu $2p_{3/2}$ intensity emitted by the oxide layer (thickness: d_{Oxide}) and attenuated by the adsorbed protein is given by:

$$I_{Cu}^{Oxide} = k\sigma_{Cu}\lambda_{Cu}^{Oxide}D_{Cu}^{Oxide}T_{Cu}\exp\left(-\frac{d_{BSA}}{\lambda_{Cu}^{BSA}}\right)\left(1-\exp\left(-\frac{d_{Oxide}}{\lambda_{Cu}^{Oxide}}\right)\right) \quad (2)$$

with D_{Cu}^{Oxide} the copper density in the oxide.

The combination of Equations (1) and (2) gives:

$$\frac{I_N^{BSA}}{I_{Cu}^{Oxide}}\times\frac{\sigma_{Cu}\lambda_{Cu}^{Oxide}D_{Cu}^{Oxide}T_{Cu}}{\sigma_N\lambda_N^{BSA}D_N^{BSA}T_N} = \frac{1-\exp\left(-\frac{d_{BSA}}{\lambda_N^{BSA}}\right)}{\exp\left(-\frac{d_{BSA}}{\lambda_{Cu}^{BSA}}\right)\left(1-\exp\left(-\frac{d_{Oxide}}{\lambda_{Cu}^{Oxide}}\right)\right)} \quad (3)$$

The values of the transmission function of the Escalab 250 energy analyser, considered for the calculations, were $T_N = 3233.4$ for nitrogen (N 1s) and $T_{Cu} = 4265.0$ for copper (Cu $2p_{3/2}$). The photo-ionisation cross-sections at 1486.6 eV were taken from Scofield [62]: $\sigma_{Cu} = 16.73$ for

Cu $2p_{3/2}$, and σ_N = 1.8 for N 1s. The inelastic mean free paths were calculated by the TPP2M formula [63]: λ_{Cu}^{Oxide} = 1.20 nm, λ_{N}^{BSA} = 3.39 nm, and λ_{Cu}^{BSA} = 1.94 nm. At last, the density values used in Equation (3) were: D_{Cu}^{Oxide} = 0.034 mol.cm^{-3}, and D_{N}^{BSA} = 0.016 mol.cm^{-3}.
The thickness estimated from XPS data for the adsorbed BSA layer is ~ 3 nm which, according to the size of the BSA molecule [38], corresponds to one monolayer. For ASW + TB EPS and ASW + LB EPS, the thickness of the adsorbed biomolecule layer was estimated from XPS data, considering the same parameter values as for the model protein (BSA). The results are d_{BSA} = 1.3 nm for TB EPS and d_{BSA} = 2.6 nm for LB EPS.

ToF-SIMS experiments and XPS spectra carried out with ASW, ASW + BSA, and ASW+TB EPS show that only oxidized species are detected on top of the sample. Assuming a continuous and homogeneous oxide layer, the composition of the oxide layer was calculated considering the intensities of copper and nickel in the mixed oxide layer (Table 4). Immersion of the alloy in the presence of BSA or TB EPS modifies the chemical composition of the surface oxide film: an important decrease of Cu^+ content together with an important increase of Cu^{2+} and Ni^{2+} concentrations can be observed. After immersion in ASW + LB EPS, metallic Cu and Ni signals have been evidenced by XPS (Figure 5). Assuming a continuous and homogeneous oxide layer, the composition and the equivalent thickness of the oxide layer and the alloy composition underneath the oxide layer can be calculated, considering the intensities of copper and nickel in the metallic substrate and in the mixed oxide layer. The following layer model was assumed: organic layer (equivalent thickness: d_{Org}) covering the mixed oxide layer (equivalent thickness: d_{Oxide}) formed on the metallic substrate. Furthermore, the Cu Auger line was used to obtain information about the relative contributions of Cu_2O, CuO and metallic Cu. For that purpose, the decomposition was performed using the reference spectra of Cu_2O, CuO and metallic Cu. The oxide layer thickness is estimated to be 1.6 nm. The composition of the alloy beneath the oxide layer is: 82 at. % Cu+ 18 at. % Ni; the composition of the oxide layer is reported in Table 4.

From combined XPS and ToF-SIMS data, the surface layers after 1h immersion at E_{corr} in the four different solutions can be represented by the models shown in Figure 6. In the absence of biomolecules (Figure 6(a)), surface analysis shows two oxidized layers: an outer layer mainly composed of cuprous oxide (redeposited Cu_2O) and an inner layer mainly composed of oxidized nickel, with a global thickness of ~ 30 nm. This duplex structure is similar to the one reported by Souchet *et al.* for the early stages (1-2 h) of CuNi alloys oxidation in air [64,65]. In our case, the duplex structure is associated to Cu_2O redeposition due to the fact that experiments were carried out in static conditions.
XPS and ToF-SIMS analyses show that biomolecules (BSA, TB EPS and LB EPS) are adsorbed on the surface. The adsorbed organic layer was found to have an equivalent thickness of ~ 3 nm for ASW + BSA and ASW + LB EPS, and only of ~ 1 nm for ASW + TB EPS. In the presence of BSA, ToF-SIMS data show that the oxide layer is partly covered by the protein; with TB EPS, the calculated value of the adlayer equivalent thickness is low meaning that the surface is probably not totally covered by biomolecules.
In the biomolecules-containing solutions, the thickness of the oxide film beneath the organic adlayer, as well as its structure and composition, are modified. The presence of BSA leads to a mixed oxide layer of ~ 10 nm composed of CuO (and maybe $Cu(OH)_2$ or $Cu(SO_4)_2$), Cu_2O, and $Ni(OH)_2$ (Figure 6(b)). Compared to the results obtained without biomolecules, there is a marked decrease of the Cu_2O content in the oxide layer.
Similarly to what is observed for static ASW + BSA, the presence of TB EPS induces the formation of a mixed oxide layer composed of Cu^+, Cu^{2+}, and Ni^{2+} compounds, but with a

lower Cu_2O content, a higher $Ni(OH)_2$ content, as well as a lower oxide layer thickness (Figure 6(c)).
Results obtained in the presence of LB EPS show a markedly thinner mixed oxide layer (~ 1.6 nm) mainly composed of Cu^{2+} and Ni^{2+} species (Figure 6(d)). Furthermore, the lowest Cu^{+} content was observed in the presence of LB EPS.

4 Discussion

4.1 Corrosion mechanism

The anodic dissolution of pure copper in acidic and neutral chloride media has been extensively studied in the literature. The final model in agreement with all published experimental data is [50,51,66-69]:

$$Cu + Cl^{-} \Leftrightarrow CuCl + e^{-} \quad (4)$$

$$CuCl + Cl^{-} \Leftrightarrow CuCl_2^{-} \quad (5)$$

In this mechanism, the soluble cuprous complex $CuCl_2^{-}$ is the diffusing species and the insoluble adsorbed intermediate CuCl is the blocking species (surface coverage: γ), which is electrochemically formed in a first step (Reaction (4)) and chemically dissolved in a second step (Reaction (5)).

From that mechanism shown for pure copper dissolution in chloride media at low anodic potential and in order to take into account the presence of an oxide layer as shown by surface analysis, a modified mechanism can be drawn for the anodic partial reaction of 70Cu-30Ni alloy at E_{corr} in ASW without and with biomolecules:

$$Cu \rightarrow Cu^{+} + e^{-} \quad \text{oxidation at the alloy/oxide interface} \quad (6)$$

$$Cu^{+}_{\text{alloy/oxide}} \rightarrow Cu^{+}_{\text{oxide/solution}} \quad \text{solid-state mass transport} \quad (7)$$

$$Cu^{+} + Cl^{-} \Leftrightarrow Cl_{ads} - Cu_{Cu_2O} \quad \text{adsorption at the oxide/solution interface} \quad (8)$$

$$Cl_{ads} - Cu_{Cu_2O} + Cl^{-} \Leftrightarrow CuCl_2^{-} \quad \text{dissolution at the oxide/solution interface} \quad (9)$$

This mechanism involves four steps: 1) oxidation of Cu as Cu^{+} at the alloy/oxide interface, 2) mass transport of Cu^{+} by diffusion and migration in the solid phase from the alloy/oxide interface to the oxide/solution interface, 3) adsorption of chloride on a Cu^{+} surface site of the Cu_2O oxide at the oxide/solution interface, and 4) dissolution of copper as $CuCl_2^{-}$ at the oxide/solution interface, followed by mass transport of $CuCl_2^{-}$ by diffusion in the liquid phase from the oxide/solution interface to the bulk solution.
In aerated solution, the cathodic partial reaction is the reduction of dissolved oxygen that takes place at the oxide/solution interface.

4.2 Analysis of impedance data

At E_{corr}, the anodic and cathodic currents have the same magnitude and the net current is equal to zero. By principles of summation of currents, the Faradaic anodic and cathodic impedances must be in parallel. The polarization curves show that both the anodic and the cathodic reactions are affected by mass transport. Therefore, the anodic Faradaic impedance can be depicted by a charge transfer resistance (R_t^a) in series with an impedance that illustrates Cu^{+} and/or $CuCl_2^{-}$ mass transport and partial blocking effect by adsorbed species, such as CuCl ($Z_{\theta,D}^a$); whereas the cathodic impedance can be depicted by a charge transfer resistance (R_t^c) in series with an impedance that illustrates O_2 mass transport (Z_D^c). A double layer capacitance C_{dl} is added in parallel with the anodic and the cathodic impedances. As the

impedance response for electrochemical systems often reflects a distribution of reactivity that is commonly represented in equivalent electrical circuits as a constant-phase element (CPE), C_{dl} is replaced here by CPE_{dl} which is a constant phase element related to the double layer. The CPE impedance is expressed in terms of model parameters α and Q as:

$$Z_{CPE}(\omega) = \frac{1}{Q(j\omega)^{\alpha}} \quad (10)$$

When $\alpha = 1$, the parameter Q has units of capacitance; otherwise, Q has units of $\Omega^{-1}.cm^{-2}.s^{\alpha}$ or $F.cm^{-2}.s^{(\alpha-1)}$. Thus, the general impedance model for 70Cu-30Ni alloy in seawater, without and with biomolecules, is illustrated in Figure 7(a), where R_e is the electrolyte resistance [40].
The cathodic polarization curves show a first current plateau for the reduction of dissolved oxygen (transfer of 2 electrons) close to E_{corr}. If it is assumed that this plateau can be extrapolated down to E_{corr} *i.e.* pure mass transport limitation for the cathodic partial reaction at E_{corr}, then R_t^c can be neglected and the cathodic mass transport impedance is a Warburg impedance (W_c) given by:

$$Z_{W_c} = 1/\left(k_c\sqrt{j\omega}\right) \quad (11)$$

with k_c expressed in $s^{0.5}.\Omega^{-1}.cm^{-2}$.Taking into account experimental cathodic polarization curves, the 70Cu-30Ni/ASW system without and with biomolecules can be modeled by the simplified circuit presented in Figure 7(b) [40].

For the same experimental impedance data as those presented in Figure 3 in the complex plane, the absolute value of the imaginary part of the impedance ($|Z_j|$) was plotted as a function of the frequency in logarithmic coordinates (Figure 8(a)) [70]. In all cases, a pseudo-straight line with a slope lower than 1 in absolute value, suggesting a CPE-like behavior, can be observed in the HF range. As this slope varies slightly with the frequency, the CPE parameter α (Eq. (10)) cannot be graphically determined from Figure 8(a), following the method presented by Orazem *et al.* [70].Therefore, to better visualize a possible constant value of the slope in a narrow frequency range, the $d\log|Z_j|/d\log f$ *vs* $\log f$ curves were calculated from those presented in Figure 8(a) (derivative curves; Figure 8(b)). In the case of R//CPE circuit, a plateau would be observed at HF corresponding to a value of $-\alpha$. In Figure 8(b), no plateau is clearly visible in any case, in particular at very HF, and again the value of α cannot be graphically obtained.
In conclusion, the HF loop of the experimental impedance diagrams cannot be modeled by a R//CPE circuit but corresponds to the $CPE_{dl}//R_t^a//W_c$ equivalent circuit (Figure 7(c)), whereas the LF loop is related to the anodic mass transport and partial blocking effect by adsorbed species ($Z_{\theta,D}^a$). The HF loop illustrates mainly the anodic charge transfer (diameter equal to R_t^a), and its depressed shape is partly due to the CPE and partly due to the cathodic Warburg impedance in parallel. Since no plateau is visible at very HF in Figure 8(b), the effect of W_c is not negligible compared to that of CPE_{dl} even at 10^4 Hz, and there is no clear frequency domain specifically assigned to each process [40].

The circuits of Figures 7(a) and (b) take into account the presence of an oxide layer, as shown by surface analysis, through $Z_{\theta,D}^a$ that partly illustrates Cu^+ mass transport within that layer.

As the LF loop of impedance diagrams is not well defined (described only by a few points in Figure 3), the single HF loop was analysed by regression of the equivalent circuit presented in Figure 7(c), using Simad® software developed at LISE (Figure 9). As shown in Figure 9, the fit is good in all cases. The regression results are presented in Table 5. The experimental

frequency ranges taken into account for the regression are also indicated in Table 5, but the fitted curves in Figure 9 are shown in the whole frequency range (0.003 Hz – 100 kHz), with parameters values corresponding to those given in Table 5.
If comparing parameters values for experiments carried out in identical conditions, the uncertainty on R_e is lower than 5%, that on R_t^a is lower than15%, that on k_c is lower than 15%, that on α is lower than 5%, and that on Q is lower than 50%. Thus, the highest uncertainty is obtained for Q.

If the CPE behaviour is assumed to be associated with surface distributed time constants for charge-transfer reactions (time-constant distribution along the electrode surface), then it is possible to apply the equation derived by Brug *et al*. to calculate the effective capacitance associated with the CPE [71,72]:

$$C_{eff} = Q^{1/\alpha}\left(R_e^{\ -1} + R_t^{a\,-1}\right)^{(\alpha-1)/\alpha} \tag{12}$$

The capacitance values calculated from the impedance diagrams shown in Figure 3, taking for R_e and R_t^a the values extracted from the regression procedure (Table 5), are also given in Table 5. As a result of the uncertainties on α, Q, R_e and R_t^a, the uncertainty on C_{eff} is lower than 30%. These capacitance values, of the order of several tens of μF.cm^{-2}, are typical of those for a double layer capacitance, which validates the equivalent circuits proposed in Figure 7. If a layer thickness (δ) was calculated from C_{eff} by application of $C_{eff} = \varepsilon\varepsilon_0/\delta$ with ε the dielectric constant of the layer and ε_0 the vacuum permittivity, a value of a few Å would be obtained for δ with $\varepsilon = 18$ (dielectric constant found for CuO), which is too low to be an oxide layer thickness (rather a few nm; see Figure 6). This confirms that C_{eff} is well related to the double layer and not to the oxide film. Therefore, the HF loop illustrates mainly the anodic charge transfer and its diameter is equal to R_t^a.
The C_{eff} value calculated for ASW + TB EPS is similar to the value obtained without biomolecules and seems to be higher than the ones calculated for the other biomolecules. This can be explained by a blocking effect by the adsorbed organic layer in the case of BSA and LB EPS, which decrease the active surface area (S_{act}) where the electron transfer occurs. Thus, the C_{eff} ratio without and with biomolecules would be equal to the active surface ratio:

$$\frac{C_{eff}^{without}}{C_{eff}^{with}} = \frac{S_{act}^{without}}{S_{act}^{with}} \tag{13}$$

The mean value for this ratio is about 1.3. This blocking effect in the presence of BSA and LB EPS is in agreement with a higher equivalent thickness of the adsorbed organic layer estimated from XPS data in these two cases (3 nm for ASW + BSA and ASW + LB EPS to be compared to 1 nm for ASW + TB EPS). This result could also be linked to a lower amount of adsorbed proteins in the presence of TB EPS compared to LB EPS and BSA (similar amount for LB EPS and BSA; results deduced from a deep analysis of XPS data, not shown here).

Compared to the value obtained in static ASW without biomolecules, R_t^a is ~ 22 % higher in the presence of BSA, ~ 6.5 % higher in the presence of TB EPS, and ~ 150 % higher in the presence of LB EPS.
For a reaction dependent on potential and mass transport (the surface coverage by CuCl is neglected *i.e.* $\gamma << 1$, which is true at E_{corr}), the anodic charge transfer resistance R_t^a is defined as [73]:

$$R_t^a = \frac{1}{nFke^{b(V-V_0)}bC^0} \qquad \text{with} \qquad b = \frac{\alpha nF}{RT} > 0 \tag{14}$$

where n is the number of transferred electrons (n = 1 in Reaction (4)), k the rate constant of the reaction, α the symmetry factor, V the interfacial potential, V_0 the interfacial equilibrium potential and C^0 the surface concentration of the diffusing species ($CuCl_2^-$ for copper alloys). Thus, mass transport influences charge transfer by means of the surface concentration.
In static conditions, changes in R_t^a value can be explained by three different effects: 1) a potential effect (V in Eq. (14)), 2) a kinetic effect (k in Eq. (14)), and 3) a blocking or surface effect induced by the adsorbed biomolecules. If we assume constant b, constant V_0 and constant C_0 without and with biomolecules, then Eq. (14) becomes:

$$\frac{R_t^a\Big|^{with}}{R_t^a\Big|^{without}} = \frac{k^{without}}{k^{with}} \times e^{b(E_{corr}^{without} - E_{corr}^{with})} \times \frac{S_{act}^{without}}{S_{act}^{with}} \tag{15}$$

where R_t^a is expressed in Ω. Given Eq. (13), Eq. (15) can be written as:

$$\frac{k^{without}}{k^{with}} = \frac{R_t^a\Big|^{with}}{R_t^a\Big|^{without}} \times e^{b(E_{corr}^{with} - E_{corr}^{without})} \times \frac{C_{eff}^{with}}{C_{eff}^{without}} \tag{16}$$

In chloride media and at low anodic potential, pure copper dissolution involves Cu^+ species (Reactions (4) and (5)). If the same mechanism is assumed for the anodic partial reaction of 70Cu-30Ni alloy immersed at E_{corr} in ASW, then n can be taken as 1. Moreover, α is comprised between 0 and 1, and is usually assumed to be equal to 0.5. Therefore, $b \approx 20$ and the numeral application of Eq. (16) gives $\frac{k^{without}}{k^{with}}(BSA) = 1.7$, $\frac{k^{without}}{k^{with}}(TB\ EPS) = 2.1$, and $\frac{k^{without}}{k^{with}}(LB\ EPS) = 3.2$. In all cases, $k^{without} > k^{with}$ which means that the anodic reaction is slown down by the biomolecules and the effect of potential is compensated by a strong kinetic effect. Indeed, as E_{corr} is more anodic in the presence of biomolecules and almost constant for the 3 biomolecules, a single effect of the potential would induce a decrease of R_t^a (see Eq. (14)). This kinetic effect is the strongest in the case of LB EPS.

Under assumption of Tafel kinetics (pure kinetic control) for the anodic partial reaction, the corrosion current density j_{corr} is related to R_t^a and the anodic Tafel slope β_a by [74]:

$$j_{corr} = \frac{1}{b \times R_t^a} \tag{17}$$

In Table 6, the j_{corr} values calculated by application of Eq. (17), with n = 1 and α = 0.5, are compared to those deduced graphically from the cathodic polarisation curves, taking into account the first plateau current density in the case of ASW, ASW + BSA AND ASW + TB EPS, or an extrapolation of the cathodic pseudo straight line down to E_{corr} in the case of ASW + LB EPS. As a result of the uncertainty on R_t^a, the uncertainty on calculated j_{corr} is lower than 20%. If considering ASW, ASW + BSA and ASW + TB EPS, for which j_{corr} values can be more easily extracted from the cathodic polarisation curves, there is quite a good agreement between the values obtained from Eq. (17) and those deduced graphically. The ratio of about 2-3 between both kinds of values may be partly explained by a value of α

different from 0.5 and partly explained by the fact that the cathodic polarisation curves plotted in Figure 2(a) are not steady-state curves (scan rate of 0.5 $mV.s^{-1}$), which is of particular concern near the corrosion potential due to the presence of an oxide layer. It was shown that quasi steady-state cathodic polarisation curves yield first plateau current densities higher than those deduced from non steady-state curves (results not presented here).
The corrosion current density of 70Cu-30Ni alloy after 1 h of immersion in static ASW is slightly lower with BSA and similar with TB EPS compared to that estimated in the absence of biomolecules. A significant decrease of j_{corr} value is observed in the presence of LB EPS. Therefore, these results show a clear corrosion inhibition effect for LB EPS, a small beneficial effect for BSA and no detrimental effect for TB EPS.

4.3 Conclusions deduced from combined electrochemical measurements and surface analysis

It has been shown from impedance data in static conditions a slow-down of the anodic reaction by the biomolecules (BSA, TB EPS and LB EPS), and a corrosion inhibition effect by LB EPS and to a lesser extent by BSA.
This slow-down/inhibition of the anodic dissolution by the biomolecules can then give rise to two different cases: (i) either the amount of dissolved Cu^+ is below the solubility limit of Cu^+, and in that case, no redeposition of Cu_2O occurs, or (ii) the amount of dissolved Cu^+ is above the solubility limit of Cu^+, and in that case, adsorbed biomolecules inhibit Cu_2O redeposition by blocking the surface.
The kinetic effect and corrosion inhibition effect are the strongest in the case of LB EPS, in agreement with the lowest Cu^+ content in the oxide layer, the lowest oxide layer thickness and a low amount of Cl^--containing species in the surface layers, estimated from ToF-SIMS and XPS data. Therefore, combined electrochemical measurements and surface analysis in static ASW show that adsorbed LB EPS inhibit the corrosion of 70Cu-30Ni alloy and suppress Cu_2O redeposition (amount of dissolved Cu^+ below the solubility limit),whereas adsorbed BSA and TB EPS slow-down the anodic dissolution (kinetic effect) and inhibit Cu_2O redeposition (surface blocking effect). This surface blocking effect is the weakest in the presence of TB EPS.
These differences in the electrochemical behavior and the surface chemical composition observed in the various solutions might be explained by differences in the chemical composition of adsorbed organic layers. Beech *et al*. showed by XPS that conditioning layers formed upon exposure of AISI 316 stainless steel to EPS solutions (planktonic, capsular and biofilm EPS) were chemically dissimilar [17].

5 Conclusions

Loosely bound EPS (LB EPS) and tightly bound EPS (TB EPS) were extracted from a marine aerobic strain of *Pseudomonas*, *Pseudomonas* NCIMB 2021, and their composition in proteins, sugars, DNA and uronic acids was determined. Differences in bulk composition are detected depending on the kind of EPS: LB EPS contain more sugars than proteins, and TB EPS are highly concentrated in proteins.
The influence of these EPS on the electrochemical behaviour of 70Cu-30Ni alloy and the chemical composition of oxide layers was studied in static aerated artificial seawater (ASW) by combined electrochemical measurements and surface analysis.Results were compared with those obtained in ASW with 20 $mg.L^{-1}$ of BSA (model protein).
From XPS and ToF-SIMS data, a thick duplex oxide layer, with an outer Cu_2O redeposited layer and an inner oxidized nickel layer, is shown in the absence of biomolecules, whereas a mixed oxide layer (oxidized copper and nickel) with a lower thickness is evidenced in the

presence of BSA, TB EPS and LB EPS. The Cu^+ content in the oxide layer and the oxide layer thickness are the lowest with LB EPS. In the biomolecules-containing solutions, this oxide layer is covered by an adsorbed organic layer, mainly composed of proteins, with an equivalent thickness similar for BSA and LB EPS (~ 3 nm), and lower for TB EPS (~ 1 nm).
A model is proposed to analyse electrochemical impedance data obtained at E_{corr}. This model assumes that:

a) the anodic partial reaction involves the dissolution of Cu as Cu^+ species (modified mechanism drawn from that for pure Cu dissolution in chloride media at low anodic potential);
b) the cathodic partial reaction is the oxygen reduction reaction (aerated solutions);
c) the anodic and the cathodic partial reactions are affected by mass transport, with pure mass transport limitation for the cathodic partial reaction, and mixed kinetic control for the anodic partial reaction;
d) the anodic partial current is limited by the mass transport of Cu^+ in the solid phase and of $CuCl_2^-$ in the electrolyte.

The fitting procedure of impedance data allows extracting the anodic charge transfer resistance (diameter of the high frequency loop), from which the corrosion current density can be calculated. The results show a slow-down of the anodic reaction in the presence of biomolecules (BSA, TB EPS and LB EPS), and a corrosion inhibition effect by LB EPS and to a lesser extent by BSA. No detrimental effect is evidenced with TB EPS.
These differences in electrochemical behavior and surface chemical composition observed depending on the type of biomolecules in solution must be linked with the chemical composition in proteins, lipids and polysaccharides of the adsorbed organic layer, deduced from a deep analysis of XPS data. These results will be the purpose of a forthcoming paper.
Similar results were observed with St37–2 carbon steel in static ASW containing EPS extracted from *Desulfovibrio alaskensis* AL1 (protein concentration of 20 $mg.L^{-1}$): important corrosion inhibition effect by LB EPS, and negligible or poor corrosion inhibition effect by TB EPS [26].
Therefore, loosely bound EPS extracted from different bacterial strains are candidate compounds to be potentially used as green corrosion inhibitors of metallic materials in seawater.

Acknowledgements

The research leading to these results has received funding from the European Community's Seventh Framework Programme (FP7/2007-2013) under grant agreement n° 238579. Project website: www.biocor.eu/ip8 (RSP3).
The authors gratefully acknowledge Bernard Tribollet, at the Université Pierre et Marie Curie in Paris, for fruitful discussions about impedance results.

References

[1] C.A. Powell, H.T. Michels, Copper-nickel alloys for seawater corrosion resistance and antifouling - A state of the art review, Corrosion 2000, NACE.

[2] F. Mansfeld, G. Liu, H. Xiao, C.H. Tsai, B.J. Little, The corrosion behavior of copper alloys, stainless steels and titanium in seawater,Corros. Sci. 36(12) (1994) 2063–2095.

[3] Y.Z. Wang, A.M. Beccaria, G. Poggi, The effect of temperature on the corrosion behaviour of a 70/30 Cu-Ni commercial alloy in seawater, Corros. Sci. 36(8)(1994) 1277–1288.

[4] A.M. Alfantazi, T.M. Ahmed, D. Tromans, Corrosion behavior of copper alloys in chloride media, Mater. Des. 30(7)(2009) 2425–2430.

[5] P. Cristiani, G. Perboni, A. Debenedetti, Effect of chlorination on the corrosion behavior of CuNi 70/30 condenser tubing, Electrochim. Acta 54 (2008) 100–107.

[6] W.M. Dunne, Bacterial adhesion: seen any good biofilms lately?, Clin. Microbiol. Rev. 15 (2002) 155–166.

[7] S. Rajagopal, K.V.K. Nair, J. Azariah, G. van der Velde, H.A. Jenner, Chlorination and mussel control in the cooling conduits of a tropical coastal power station, Mar. Environ. Res. 2 (1996) 201–221.

[8] D. Thierry, W. Sand, Microbially Influenced Corrosion, in:P. Marcus(Ed.),Corrosion Mechamisms in Theory and Practice, third ed., CRC Press, Boca Raton, 2011, pp. 737–776.

[9] B. Little, P. Wagner, F. Mansfeld, Microbiologically influenced corrosion of metals and alloys, Int. Mat. Rev. 36(6)(1991) 253–272.

[10] B.H.A. Rehm, Bacterial polymers: biosynthesis, modifications and applications, Nat. Rev. Microbiol. 8 (2010) 578–592.

[11] E. Karatan, P. Watnick, Signals, regulatory networks, and materials that build and break bacterial biofilms, Microbiol. Mol. Biol. Rev. 73 (2009) 310–347.

[12] T.R. Neu, K.C. Marshall, Microbial “footprints” - A new approach to adhesive polymers, Biofouling 3 (1991) 101–112.

[13] I.B. Beech, C.W.S. Cheung, Interactions of exopolymers produced by sulphate-reducing bacteria with metal ions, Int. Biodeterior. Biodegrad. 35 (1995) 59–72.

[14] I.B. Beech, J.A. Sunner, K. Hiraoka, Microbe-surface interactions in biofouling and biocorrosion processes, Int. Microbiol. 8 (2005) 157–168.

[15] H.–C. Flemming, J. Wingender, The biofilm matrix, Nat. Rev. Microbiol. 8 (2010) 623–633.

[16] I. Beech, L. Hanjagsit, M. Kalaji, A.L. Neal, V. Zinkevich, Chemical and structural characterization of exopolymers produced by *Pseudomonas* sp. NCIMB 2021 in continuous culture, Microbiology 145 (1999) 1491–1497.

[17] I.B. Beech, R. Gubner, V. Zinkevich, L. Hanjangsit, R. Avci, Characterisation of Conditioning Layers Formed by Exopolymeric Substances of *Pseudomonas* NCIMB 2021 on Surfaces of AISI 316 Stainless Steel, Biofouling 16(2-4) (2000) 93–104.

[18] G.G. Geesey, L. Jang, J.G. Jolley, M.R. Hankins, T. Iwaoka, P.R. Griffiths, Binding of Metal Ions by Extracellular Polymers of Biofilm Bacteria, Wat. Sci. Tech. 20(11–12)(1988) 161–165.

[19] S. Comte, G. Guibaud, M. Baudu, Biosorption properties of extracellular polymeric substances (EPS) resulting from activated sludge according to their type: Soluble or bound, Process Biochem. 41 (2006) 815–823.

[20] H.H.P. Fang, L.–C. Xu, K.–Y. Chan, Effects of toxic metals and chemicals on biofilm and biocorrosion, Water Res. 36 (2002) 4709–4716.

[21] Z.H. Dong, T. Liu, H.F. Liu, Influence of EPS isolated from thermophilic sulphate–

reducing bacteria on carbon steel corrosion, Biofouling 27 (2011) 487–495.

[22] J. Busalmen, M. Vázquez, S. de Sánchez, New evidences on the catalase mechanism of microbial corrosion, Electrochim. Acta 47 (2002) 1857–1865.
[23] H.A. Videla, L.K. Herrera, Understanding microbial inhibition of corrosion. A comprehensive overview, Int. Biodeterior. Biodegrad. 63 (2009) 896–900.
[24] R. Stadler, W. Fuerbeth, K. Harneit, M. Grooters, M. Woellbrink, W. Sand, First evaluation of the applicability of microbial extracellular polymeric substances for corrosion protection of metal substrates, Electrochim. Acta 54 (2008) 91–99.
[25] A.J. Wikieł, I. Datsenko, M. Vera, W. Sand, Impact of *Desulfovibrio alaskensis* biofilms on corrosion behaviour of carbon steel in marine environment, Bioelectrochemistry 97 (2014) 52–60.
[26] A. J. Wikieł, Role of extracellular polymeric substances on biocorrosion initiation or inhibition, PhD, Universität Duisburg-Essen, Germany, 2013.
[27] K.C. Marshall, Biofilms: an overview of bacterial adhesion, activity, and control at surfaces, ASM News, 58 (1992) 202–207.
[28] M.J. Brown, N.J. Lester, Comparison of Bacterial Extracellular Polymer Extraction Methods, Appl. Environ. Microbiol. 40(2) (1980)179–185.
[29] J. Azeredo, V. Lazarova, R. Oliveira, Methods to extract the exopolymeric matrix from biofilms: A comparative study, Water Sci. Technol. 39(7) (1999) 243–250.
[30] P. d'Abzac, F. Bordas, E. van Hullebusch, P.N.L. Lens, G. Guibaud, Effects of extraction procedures on metal binding properties of extracellular polymeric substances (EPS) from anaerobic granular sludges, Colloids Surfaces B Biointerfaces 80(2) (2010) 161–168.
[31] M. Fletcher, G.G. Floodgate, An electron microscopic demonstration of an acidic polysaccharide involved in the adhesion of a marine bacterium to solid surfaces, *J. Gen. Microbiol.* 74 (1973) 325–334.
[32] M. Fletcher, G.G. Floodgate, The adhesion bacteria to solid surfaces, in: R. Fuller, D.L. Lovelock (Eds.), Microbial ultrastructure, Academic Press Incorporated, London, 1976, pp. 101–107.
[33] M. Fletcher, The effect of culture concentration and age, time and temperature on bacterial attachment to polystyrene, Can. J. Microbiol. 23 (1977) 1–6.
[34] M. Fletcher, G.I. Loeb, Influence of substratum characteristics on the attachment of a marine *Pseudomonas* to solid surfaces, Appl. Environ. Microbiol. 37 (1979) 67–72.
[35] B.E. Christensen, J. Kjosbakken, O. Smidsrod, Partial and physical characterisation of two extracellular polysaccharides produced by marine, periphytic *Pseudomonas* strain NCIMB 2021, Appl. Environ. Microbiol. 50(4) (1985) 837–845.
[36] M. Fletcher, J.M. Lessmann, G.I. Loeb, Bacterial surface adhesives and biofilm matrix polymers of marine and freshwater bacteria, Biofouling 4 (1991) 129–140.
[37] T. Peters, Serum albumin, Adv. Protein Chem. 37 (1985) 161–245.
[38] D.C. Carter, J.X. Ho, Structure of serum albumin, Adv. Protein Chem. 45 (1994) 153–205.
[39] I. Frateur, J. Lecœur, S. Zanna, C.-O. A. Olsson, D. Landolt, P. Marcus, Adsorption of BSA on passivated chromium studied by a flow-cell EQCM and XPS, Electrochim. Acta 52 (2007) 7660–7669.
[40] B.E. Torres Bautista, M.L. Carvalho, A. Seyeux, S. Zanna, P. Cristiani, B. Tribollet, P. Marcus, I. Frateur, Effect of protein adsorption on the corrosion behaviour of 70Cu-30Ni alloy in artificial seawater, Bioelectrochemistry 97 (2014) 34–42.
[41] A. Ithurbide, I. Frateur, A. Galtayries, P. Marcus, XPS and flow-cell EQCM study of albumin adsorption on passivated chromium surfaces: Influence of potential and pH, Electrochim. Acta 53 (2007) 1336–1345.

[42] V. Payet, S. Brunner, A. Galtayries, I. Frateur, P. Marcus, Cleaning of albumin−contaminated Ti and Cr surfaces: an XPS and QCM study, Surf. Interface Anal. 40 (2008) 215−219.
[43] B. Frølund, R. Palmgren, K. Keiding, P.H. Nielsen, Extraction of extracellular polymers from activated sludge using a cation exchange resin, Water Res. 30 (1996) 1749–1758).
[44] M. Dubois, K.A. Gilles, J.K. Hamilton, P.A. Rebers, F. Smith, Colorimetric Method for Determination of Sugars and Related Substances, Anal. Chem. 28(3) (1956) 350–356.
[45] T.M.C.C. Filisetti-Cozzi, N.C. Carpita, Measurement of uronic acids without interference from neutral sugars, Anal. Biochem. 197(1) (1991) 157–162.
[46] K. Burton, A study of the conditions and mechanism of the diphenylamine reaction for the colorimetric estimation of deoxyribonucleic acid., Biochem. J. 62(2) (1956) 315–323.
[47] M.M. Bradford, A rapid and sensitive method for the quantitation of microgram quantities of protein utilizing the principle of protein-dye binding, Anal. Biochem. 72(1–2) (1976) 248–254.
[48] Y.D. Karkhanis, J.Y. Zeltner, J.J. Jackson, D.J. Carlo, A new and improved microassay to determine 2-keto-3-deoxy-octonate in lipopolysaccharide of gram-negative bacteria, Anal. Biochem. 85(2) (1978) 595–601.
[49] S.M. Aljanabi, I. Martinez, Universal and rapid salt–extraction of high quality genomic DNA for PCR–based techniques, Nucleic Acids Res. 25 (1997) 4692–4693.
[50] O.E. Barcia, O.R. Mattos, N. Pébère, B. Tribollet, Study for the electrodissolution of copper in 1M hydrochloric acid solution by impedance, J. Electrochem. Soc. 140(10) (1993) 2825–2832.
[51] E. D'Elia, O.E. Barcia, O.R. Mattos, N. Pébère, B. Tribollet, High-Rate Copper Dissolution in Hydrochloric Acid Solution, J. Electrochem. Soc. 143(3) (1996) 961–967.
[52] C.D. Wagner, W.M. Riggs, L.E. Davis, J.F. Moulder, Handbook of X-ray Photoelectron Spectroscopy, Perkin-Elmer Corporation, 1979, p. 192.
[53] S.K. Chawla, N. Sankarraman, J.H. Payer, Diagnostic spectra for XPS analysis of Cu-O-S-H compounds, J. Electron Spectros. Relat. Phenomena 61(1) (1992) 1–18.
[54] M.C. Biesinger, L.W.M. Lau, A.R. Gerson, R.S.C. Smart, Resolving surface chemical states in {XPS} analysis of first row transition metals, oxides and hydroxides: Sc, Ti, V, Cu and Zn, Appl. Surf. Sci. 257(3) (2010) 887–898.
[55] G. Deroubaix, P. Marcus, X-ray photoelectron spectroscopy analysis of copper and zinc oxides and sulphides, Surf. Interface Anal. 18(1) (1992) 39–46.
[56] Y.Z. Wang, A.M. Beccaria, G. Poggi, The effect of temperature on the corrosion behaviour of a 70/30 Cu-Ni commercial alloy in seawater, Corros. Sci. 36(8) (1994) 1277–1288.
[57] A. Galtayries, J. Grimblot, J.-P. Bonnelle, Interaction of SO_2 with different polycrystalline Cu, Cu_2O and CuO surfaces, Surf. interface Anal. 24(5) (1996) 345–354.
[58] A. Galtayries, J.-P. Bonnelle, XPS and ISS Studies on the interaction of H_2S with polycrystalline Cu, Cu_2O and CuO Surfaces, Surf. Interface Anal. 23 (1995) 171–179.
[59] M.J. Genet, C.C. Dupont-Gillain, P.G. Rouxhet, XPS analysis of biosystems and biomaterials, in: E. Matijevic (Ed.), Medical Applications of Colloids, Springer Science, New York, 2008, pp. 177–307.
[60] S. Zanna, C. Compère, P. Marcus, XPS characterisation of BSA adsorption on stainless steel, in: P. Marcus, V. Maurice (Eds.), Passivation of Metals and Semiconductors, and Properties of Thin Oxide Layers, Elsevier B.V., 2006, pp. 365–370.
[61] L. Lartundo-Rojas, Influence de l'adsorption de protéine (BSA) sur le comportement électrochimique et la composition de surface d'un alliage Fe-17Cr en solution aqueuse, PhD, Université Pierre et Marie Curie, France, 2007.

[62] J.H. Scofield, Hartree-slater subshell photoionization cross-sections at 1254 and 1487 eV, J. Electron Spectrosc. 8 (1976) 129–137.
[63] S. Tanuma, C.J. Powell, D.R. Penn, Calculations of electron inelastic mean free paths II. Data for 27 elements over the 50-2000eV range, Surf. Interface Anal. 17 (1991) 911–926.
[64] R. Souchet, F. Danoix, A. D'Huysser, M. Lenglet, APFIM and XPS study of the first stages of low temperature air oxidation of industrial CuNi alloys, Appl. Surf. Sci. 87-88 (1995) 271–278.
[65] R. Souchet, M. Lenglet, P. Miché, S. Weber, S. Scherrer, Study of copper-nickel alloy oxidation by FTIR and SIMS, Analusis 21 (1993) 173–176.
[66] C. Deslouis, B. Tribollet, G. Mengoli, M.M. Musiani, Electrochemical behaviour of copper in neutral aerated chloride solution. I. Steady-state investigation, J. Appl. Electrochem. 18 (1988) 374–383.
[67] C. Deslouis, B. Tribollet, G. Mengoli, M.M. Musiani, Electrochemical behaviour of copper in neutral aerated chloride solution. II. Impedance investigation, J. Appl. Electrochem. 18 (1988) 384–393.
[68] J.-P. Diard, J.-M. Le Canut, B. Le Gorrec, C. Montella, Copper electrodissolution in 1 M HCl at low current densities. I. General steady-state study, Electrochim. Acta 43 (1998) 2469–2483.
[69] J.-P. Diard, J.-M. Le Canut, B. Le Gorrec, C. Montella, Copper electrodissolution in 1 M HCl at low current densities. II. Electrochemical impedance spectroscopy study, Electrochim. Acta 43 (1998) 2485–2501.
[70] M.E. Orazem, N. Pébère, B. Tribollet, Enhanced graphical representation of electrochemical impedance data, J. Electrochem. Soc. 153 (2006) B129–B136.
[71] G.J. Brug, A.L.G. van den Eeden, M. Sluyters-Rehbach, J.H. Sluyters, The analysis of electrode impedances complicated by the presence of a constant phase element, J. Electroanal. Chem. 176 (1984) 275–295.
[72] B. Hirschorn, M.E. Orazem, B. Tribollet, V. Vivier, I. Frateur, M. Musiani, Determination of effective capacitance and film thickness from constant-phase-element parameters, Electrochim. Acta 55 (2010) 6218–6227.
[73] M.E. Orazem, B. Tribollet, Electrochemical Impedance Spectroscopy, The Electrochemical Society Series, John Wiley & Sons, Inc., Hoboken, NJ, 2008.
[74] I. Epelboin, C. Gabrielli, M. Keddam, H. Takenouti, Electrochemical Corrosion Testing, ASTM STP 727, F. Mansfeld, U. Bertocci (Eds.), American Society for Testing and Materials, 1981, p. 150.

Tables

Table 1: Composition of EPS extracted from *Pseudomonas* NCIMB 2021 marine strain and of the negative control (sterile growth medium).

Composition ($mg.L^{-1}$)	**Proteins**	**Sugars**	**DNA**	**Uronic acids**
Negative control	9.3	89.7	0.4	3.7
Tightly bound EPS	4187.6	640.1	1.0	25.0
Loosely bound EPS	20.6	50.0	0.3	4.0

Table 2: Corrosion potential values for 70Cu-30Ni alloy after 1 h of immersion in static aerated ASW without and with biomolecules (protein concentration: 20 $mg.L^{-1}$).

	E_{corr} / V *vs* SCE
ASW	-0.230 ± 0.009
ASW + BSA	-0.203 ± 0.005
ASW + TB EPS	-0.199 ± 0.005
ASW + LB EPS	-0.203 ± 0.007

Table 3: Atomic ratios calculated from the XPS N 1s and C 1s core level spectra recorded for 70Cu-30Ni after 1 h of immersion at E_{corr} in static aerated ASW, without and with biomolecules (BSA, TB EPS, LB EPS; protein concentration: 20 mg.L^{-1}). The data recorded for BSA powder are included for comparison.

	N/C_{total}	$N/(C_2+C_3)$	C_1/C_{total}	C_2/C_{total}	C_3/C_{total}
BSA powder	0.22	0.48	0.54	0.26	0.20
ASW	0.03	0.14	0.78	0.13	0.09
ASW+BSA	0.20	0.45	0.56	0.22	0.22
ASW + TB EPS	0.15	0.35	0.57	0.22	0.21
ASW + LB EPS	0.23	0.43	0.46	0.28	0.25

Table 4: Atomic composition of the surface oxide layer calculated from XPS data recorded for 70Cu-30Ni after 1 h of immersion at E_{corr} in static aerated ASW, without and with biomolecules (BSA, TB EPS, LB EPS; protein concentration: 20 mg.L^{-1}).

	at. % Cu^{2+}	**at. % Cu^{+}**	**at. % Ni^{2+}**
ASW	0	93	7
ASW + BSA	33	16	51
ASW + TB EPS	27	11	62
ASW + LB EPS	39	1	60

Table 5: Experimental frequency range taken into account for the regression, parameters values (electrolyte resistance R_e, anodic charge transfer resistance R_t^a, constant of the cathodic Warburg impedance k_c, and CPE parameters α and Q) obtained from the regression of the equivalent circuit presented in Figure 7(c) to the HF experimental impedance data shown in Figure 3, and effective capacitance C_{eff} associated with the CPE calculated from Eq. (12).

	Frequency range / Hz	R_e / **Ω.cm^2**	R_t^a / **Ω.cm^2**	k_c / **s$^{0.5}$.Ω^{-1}.cm^{-2}**	α	Q / **F.cm^{-2}.s$^{(\alpha-1)}$**	C_{eff} / **μF.cm^{-2}**
ASW	10^5-5.6×10^{-2}	12	1390	2.5×10^{-4}	0.78	1.99×10^{-4}	37
ASW + BSA	10^5-1.08×10^{-1}	12	1690	1.2×10^{-4}	0.76	2.03×10^{-4}	30
ASW + TB EPS	10^5-1.08×10^{-1}	12	1480	2.1×10^{-4}	0.84	1.33×10^{-4}	39
ASW + LB EPS	10^5-7.8×10^{-2}	14	3530	1.1×10^{-4}	0.82	1.13×10^{-4}	27

Table 6: Comparison of the corrosion current density values obtained from R_t^a, by application of Eq. (17) with n = 1 and α = 0.5, and those deduced graphically from the cathodic polarization curves.

	R_t^a / $\Omega.cm^2$	j_{corr} / $\mu A.cm^{-2}$	
		Eq. (17)	**Cathodic polarisation curve**
ASW	1390	36	12
ASW + BSA	1690	30	12
ASW + TB EPS	1480	34	17
ASW + LB EPS	3530	14	5

Figure captions

Figure 1: Schematic drawing of the EPS extraction procedure [26].

Figure 2: (a) Cathodic and (b) anodic polarisation curves of 70Cu-30Ni after 1 h of immersion at E_{corr} in static aerated ASW, in the absence and in the presence of biomolecules (BSA, TB EPS, LB EPS) with a protein concentration of 20 $mg.L^{-1}$. Scan rate: 0.5 $mV.s^{-1}$.

Figure 3: Experimental impedance diagrams in the complex plane (Nyquist diagrams) of 70Cu-30Ni after 1 h of immersion at E_{corr} in static aerated ASW, in the absence and in the presence of biomolecules (BSA, TB EPS, LB EPS) with a protein concentration of 20 $mg.L^{-1}$.

Figure 4: Characteristic Time-of-Flight Secondary Ions Mass Spectrometry (ToF-SIMS) depth profile (negative ions) of 70Cu-30Ni after 1 h of immersion at E_{corr} in static aerated ASW (a) without biomolecules (sputtered area: 300 x 300 μm^2), (b) with BSA (20 $mg.L^{-1}$; sputtered area: 300 x 300 μm^2), (c) with TB EPS (protein concentration: 20 $mg.L^{-1}$; sputtered area: 300 x 300 μm^2), and (d) with LB EPS (protein concentration: 20 $mg.L^{-1}$; sputtered area: 700 x 700 μm^2).

Figure 5: (a) X-ray Photoelectron Spectroscopy (XPS) Cu $2p_{3/2}$ core level spectra, (b) Cu $L_3M_{45}M_{45}$ Auger lines, XPS (c) Ni $2p_{3/2}$, (d) Cl 2p, (e) N 1s, and (f) C 1s core level spectra for 70Cu-30Ni alloy after 1 h of immersion at E_{corr} in static aerated ASW, in the absence and in the presence of biomolecules (BSA, TB EPS, LB EPS) with a protein concentration of 20 $mg.L^{-1}$.

Figure 6: Models of the surface layers deduced from combined Time-of-Flight Secondary Ions Mass Spectrometry (ToF-SIMS) and X-ray Photoelectron Spectroscopy (XPS) data for 70Cu-30Ni after 1 h of immersion at E_{corr} in static aerated ASW (a) without biomolecules, (b) with BSA (20 $mg.L^{-1}$), (c) with TB EPS (protein concentration: 20 $mg.L^{-1}$), and (d) with LB EPS (protein concentration: 20 $mg.L^{-1}$).

Figure 7: Equivalent electrical circuits to model the 70Cu-30Ni/ASW system, without and with biomolecules (BSA, TB EPS, LB EPS): (a) general circuit, (b) simplified circuit taking into account experimental cathodic polarization curves, and (c) circuit used to analyse the HF loop of experimental impedance diagrams.

Figure 8: Experimental impedance data of 70Cu-30Ni obtained at E_{corr} after 1 h of immersion in static aerated ASW, in the absence and in the presence of biomolecules (BSA, TB EPS, LB EPS) with a protein concentration of 20 $mg.L^{-1}$. (a) Imaginary part of the impedance as a function of frequency, and (b) derivative curves calculated from Figure 8(a) ($d\log|Z_j| / d\log f$ *vs* $\log f$). Same data as in Figure 3.

Figure 9: High frequency loops of Nyquist diagrams obtained for 70Cu-30Ni at E_{corr} after 1 h of immersion in static aerated ASW (a) without biomolecules, (b) with BSA (20 $mg.L^{-1}$), (c) with TB EPS (protein concentration: 20 $mg.L^{-1}$), and (d) with LB EPS (protein concentration: 20 $mg.L^{-1}$). Experimental curves and fit of the impedance model presented in Figure 7(c) to the HF data. Same data as in Figure 3.

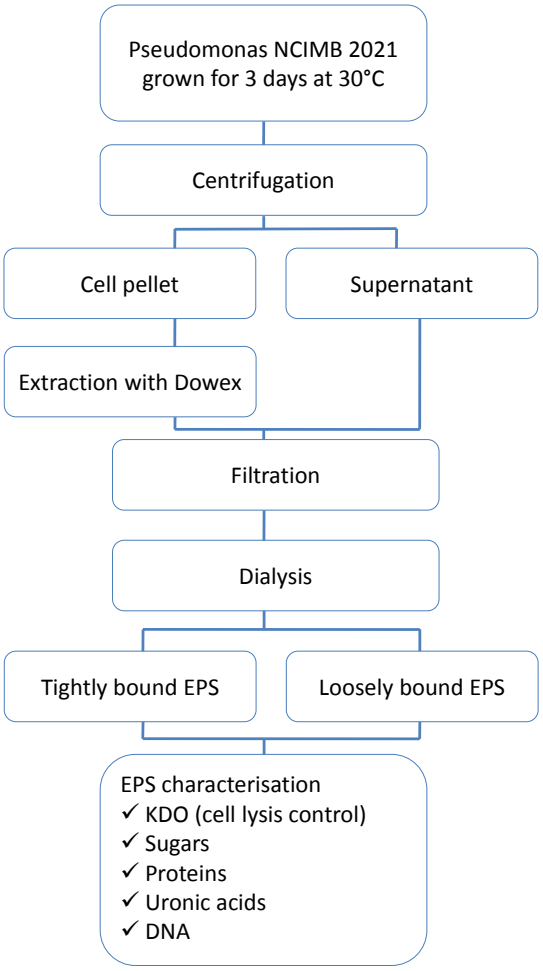
Pseudomonas NCIMB 2021 grown for 3 days at 30°C
Centrifugation
Cell pellet
Supernatant
Extraction with Dowex
Filtration
Dialysis
Tightly bound EPS
Loosely bound EPS
EPS characterisation
✓ KDO (cell lysis control)
✓ Sugars
✓ Proteins
✓ Uronic acids
✓ DNA

Figure 1

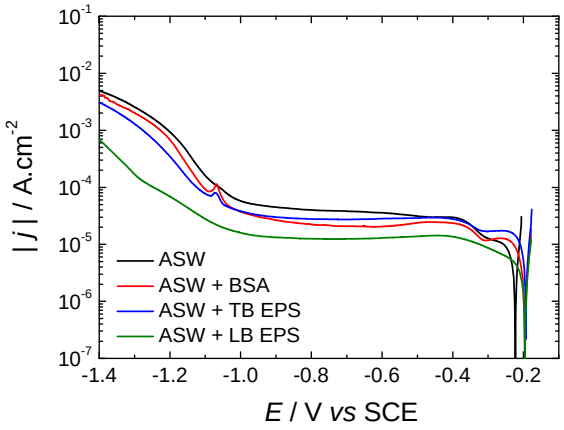
| j | / A.cm-2
E / V vs SCE
ASW
ASW + BSA
ASW + TB EPS
ASW + LB EPS

(a)

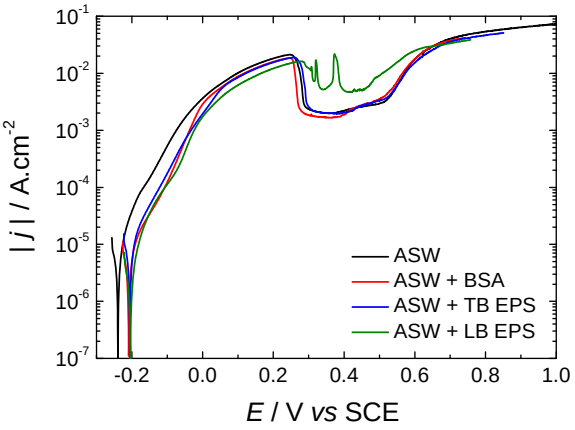
| j | / A.cm-2
E / V vs SCE
ASW
ASW + BSA
ASW + TB EPS
ASW + LB EPS

(b)

Figure 2

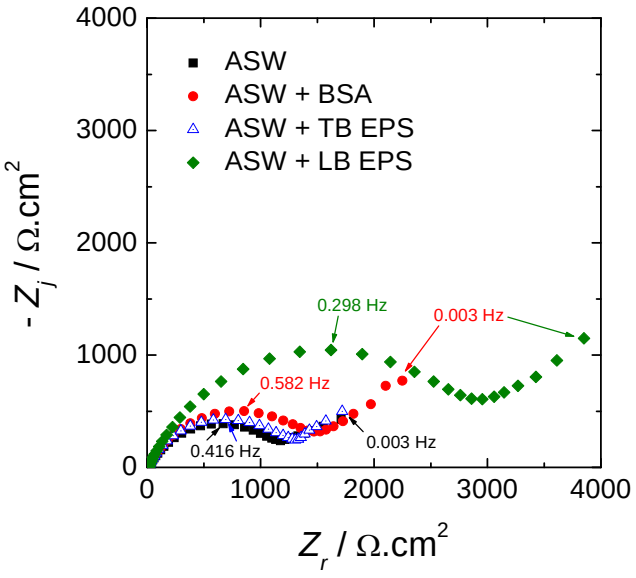
ASW
ASW + BSA
ASW + TB EPS
ASW + LB EPS
0.298 Hz
0.003 Hz
0.582 Hz
0.003 Hz
0.416 Hz
- Z_j / Ω.cm^2
Z_r / Ω.cm^2
0
1000
2000
3000
4000

Figure 3

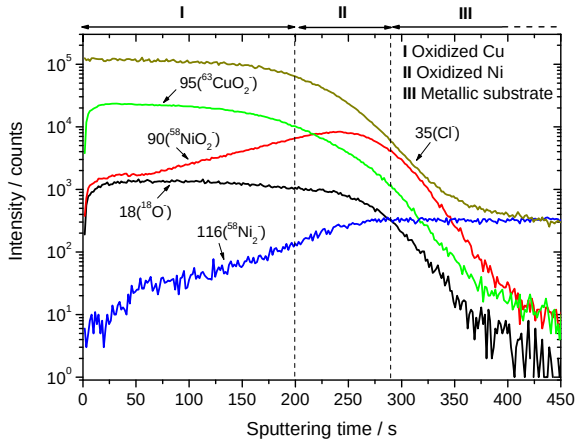

(a)

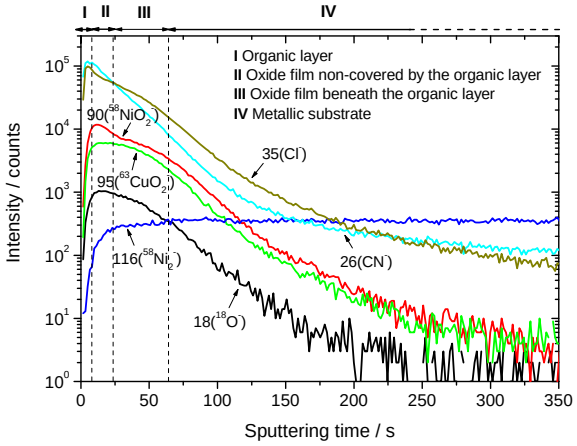

(b)

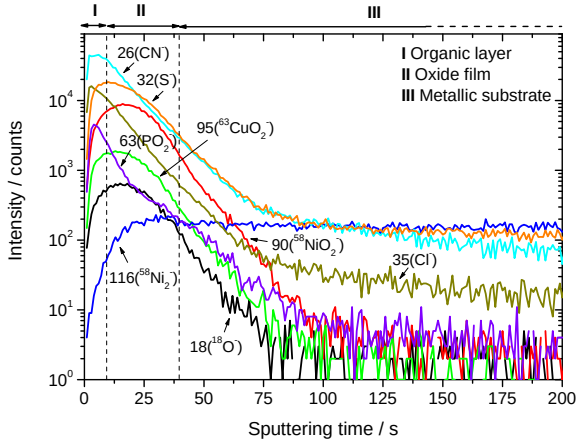

(c)

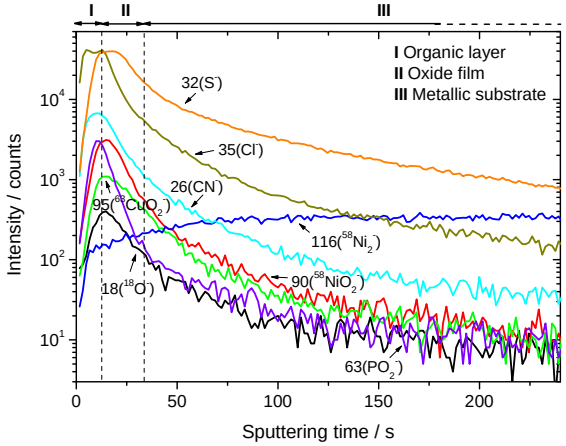

(d)

Figure 4

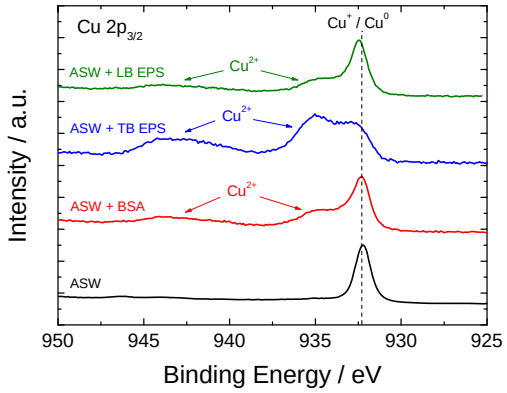

(a)

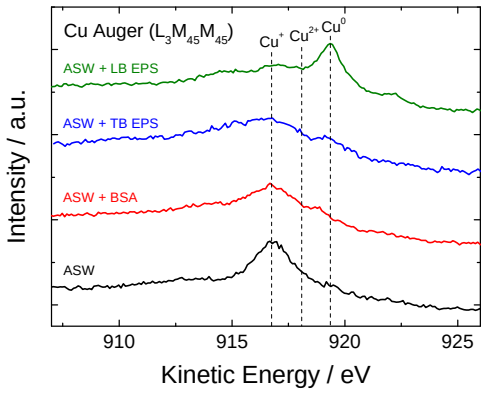

(b)

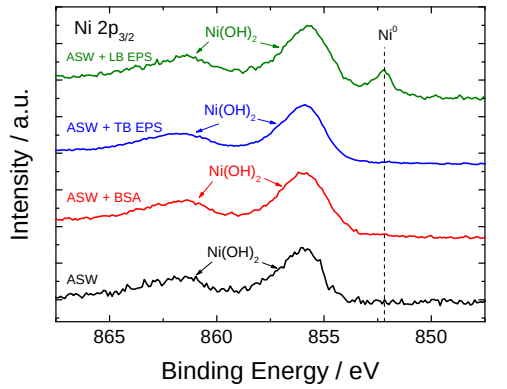

(c)

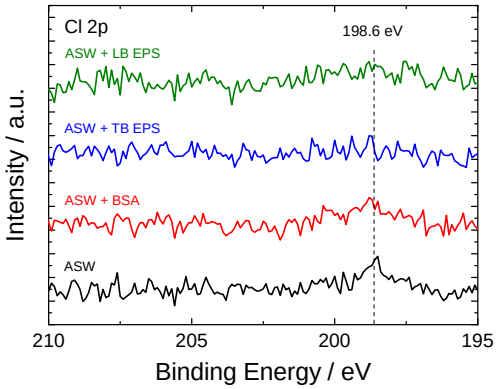

(d)

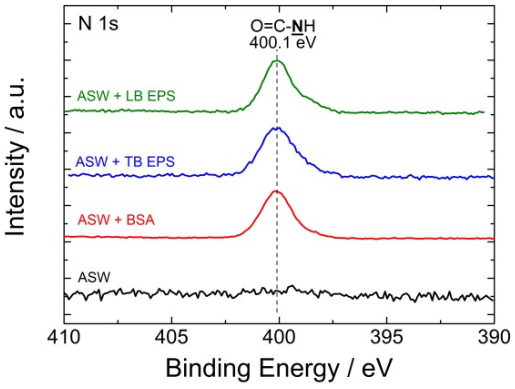

(e)

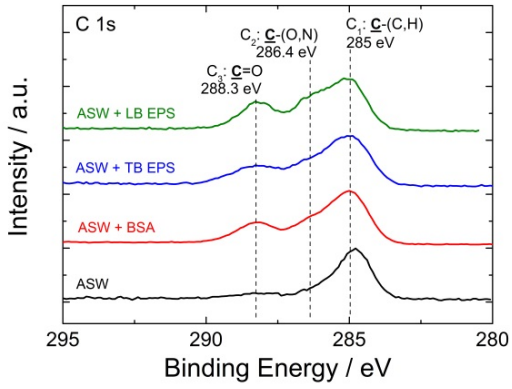

(f)

Figure 5

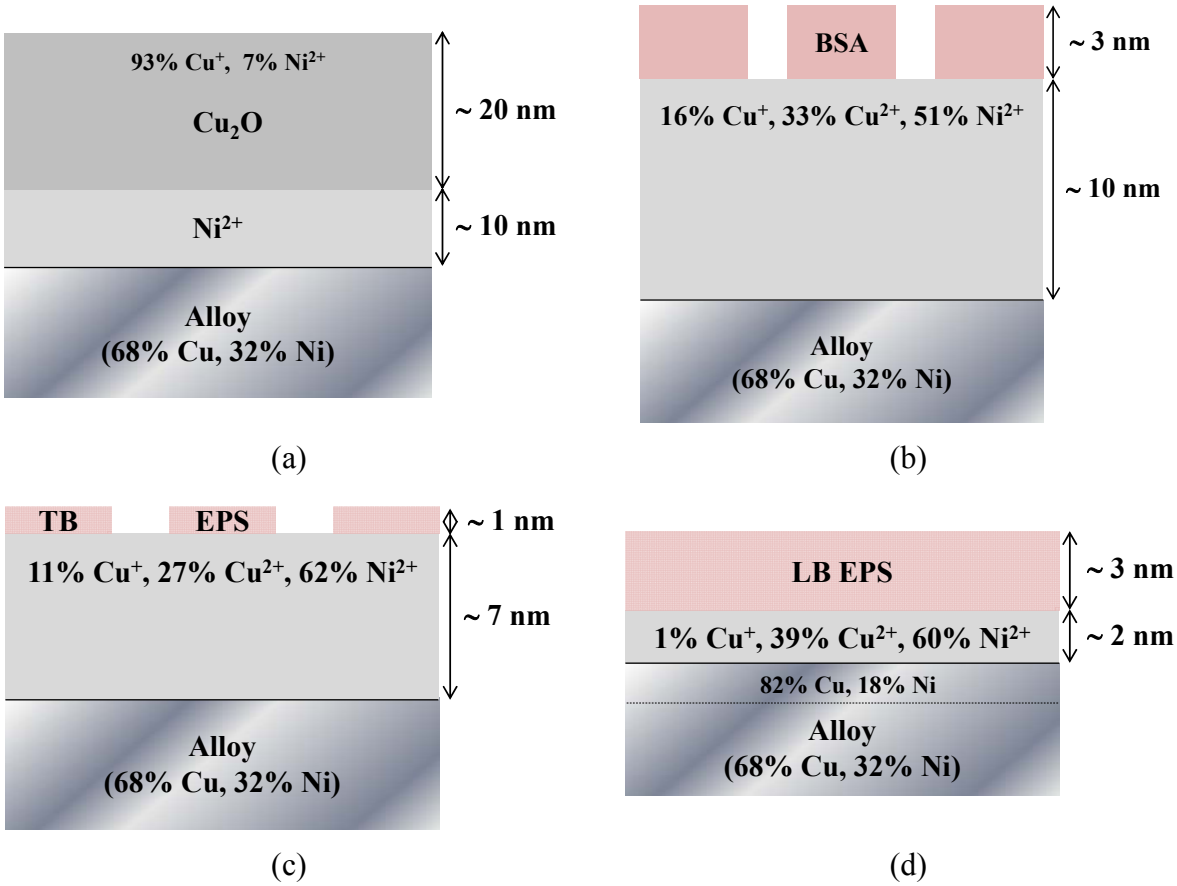
93% Cu+, 7% Ni2+
Cu2O
~ 20 nm
Ni2+
~ 10 nm
Alloy
(68% Cu, 32% Ni)
(a)
BSA
~ 3 nm
16% Cu+, 33% Cu2+, 51% Ni2+
~ 10 nm
Alloy
(68% Cu, 32% Ni)
(b)
TB
EPS
~ 1 nm
11% Cu+, 27% Cu2+, 62% Ni2+
~ 7 nm
Alloy
(68% Cu, 32% Ni)
(c)
LB EPS
~ 3 nm
1% Cu+, 39% Cu2+, 60% Ni2+
~ 2 nm
82% Cu, 18% Ni
Alloy
(68% Cu, 32% Ni)
(d)

Figure 6

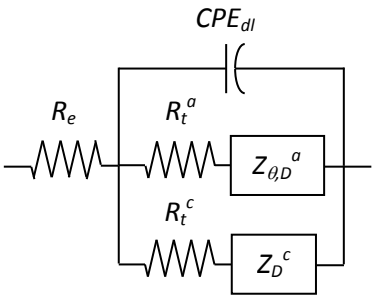
CPE_{dl}
R_e
R_t^a
$Z_{\theta,D}{}^a$
R_t^c
$Z_D{}^c$

(a)

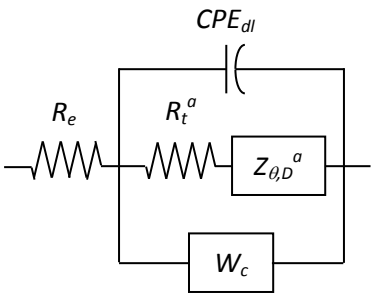
CPE_{dl}
R_e
R_t^a
$Z_{\theta,D}{}^a$
W_c

(b)

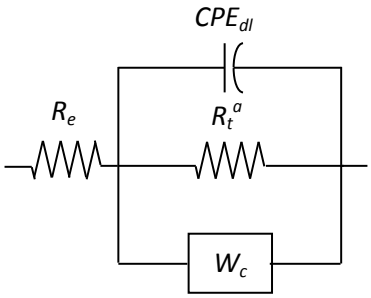
CPE_{dl}
R_e
R_t^a
W_c

(c)

Figure 7

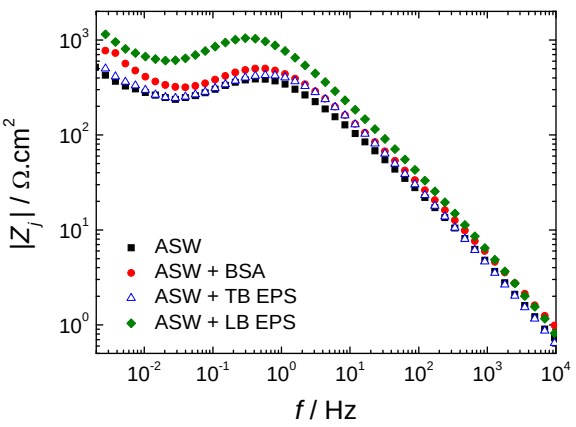
$|Z_j|$ / Ω.cm^2
f / Hz
ASW
ASW + BSA
ASW + TB EPS
ASW + LB EPS

(a)

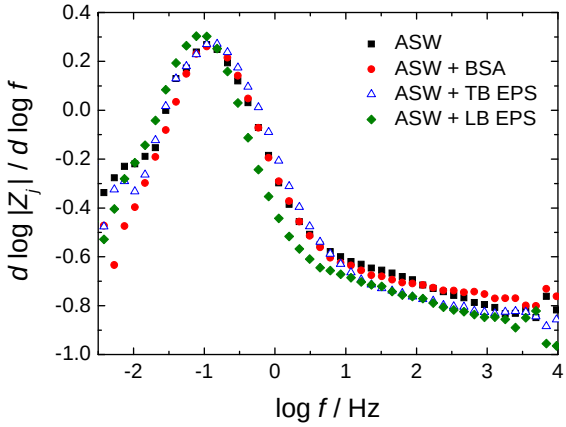
$d \log |Z_j| / d \log f$
log f / Hz
ASW
ASW + BSA
ASW + TB EPS
ASW + LB EPS

(b)

Figure 8

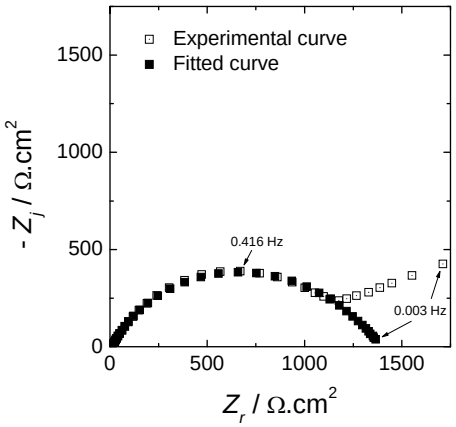
Experimental curve
Fitted curve
0.416 Hz
0.003 Hz
- Z_j / Ω.cm^2
Z_r / Ω.cm^2
0
500
1000
1500

(a)

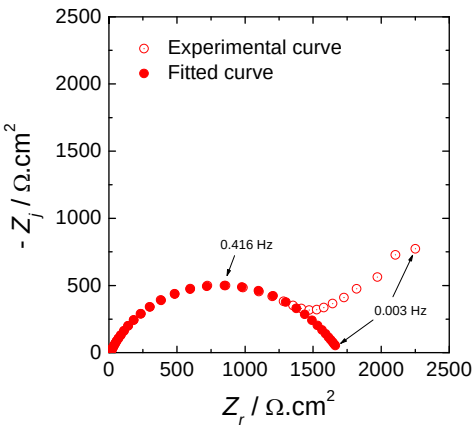
Experimental curve
Fitted curve
0.416 Hz
0.003 Hz
- Z_j / Ω.cm^2
Z_r / Ω.cm^2
0
500
1000
1500
2000
2500

(b)

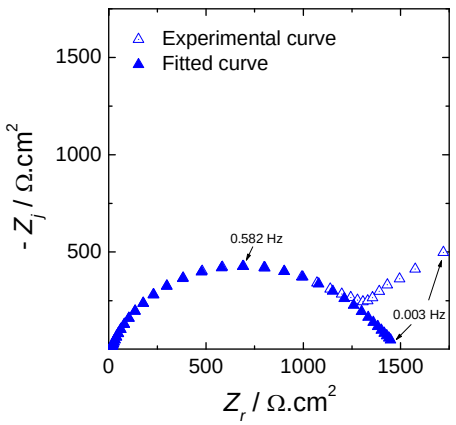
Experimental curve
Fitted curve
0.582 Hz
0.003 Hz
- Z_j / Ω.cm^2
Z_r / Ω.cm^2
0
500
1000
1500

(c)

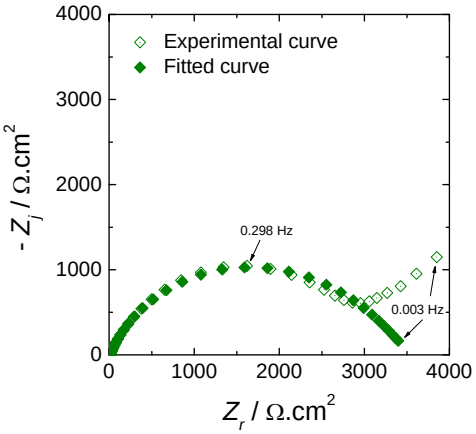
Experimental curve
Fitted curve
0.298 Hz
0.003 Hz
- Z_j / Ω.cm^2
Z_r / Ω.cm^2
0
1000
2000
3000
4000

(d)

Figure 9